Nonlinear Dyn (2019) 95:2963–2993
https://doi.org/10.1007/s11071-018-04734-4

ORIGINAL PAPER

Periodic orbits of a conservative 2-DOF vibro-impact system by piecewise continuation: bifurcations and fractals

Hongcheng Tao · **James Gibert**

Received: 17 August 2018 / Accepted: 12 December 2018 / Published online: 1 January 2019

Abstract The exact periodic orbits of a conservative 2-degree-of-freedom vibro-impact system with stereo-mechanical impact model is studied using a piecewise continuation method. Feasible initial guesses are extracted from grazing solution points so that each branch of solution can be initiated smoothly from previously solved ones. Frequency-energy plots (FEPs) are produced where an emphasis is placed on enumerating potential bifurcations. Extra critical points are discovered on multiple-period duplicates of existing stable solution branches and lead to cascades of period-multiplying bifurcations. The results indicate that the system's complete FEP can be viewed through a process of infinite fractals toward zero frequency where pseudo-periodic or chaotic responses are approached. Finally, it is shown both mathematically and through the comparison of FEPs that the impacting system can be represented explicitly as the extreme case of nonlinear systems with an odd-order polynomial internal force. It is thus proposed that as the counterpart to the superposition of linear normal modes, the free responses of a general conservative nonlinear system can be tracked via bifurcations from its nonlinear normal modes.

H. Tao (✉) · J. Gibert
Purdue University, 610 Purdue Mall, West Lafayette, IN, USA
e-mail: taoh@purdue.edu

J. Gibert
e-mail: jgibert@purdue.edu

Keywords Nonlinear normal mode · Vibro-impact system · Continuation · Fractals · Nonsmooth dynamical system

1 Introduction

Impact is an important phenomenon in mechanical systems. Severe impacts can be destructive and thus undesired during the operation of machines. Conversely, impacts can be useful in vibration absorbers, which dissipate energy by the attachment of carefully adjusted impact oscillators [1,2]. Understanding the dynamics of vibro-impact (VI) systems is essential in preventing structural instabilities as well as optimizing mechanical designs.

The main interest in the studies of VI systems lies in the strong nonlinearity that is nonsmooth in nature. However, impacts may differ according to the contact models employed [3–5], e.g., the Hertzian contact model [6], the bilinear model [7–9] as well as the stereo-mechanical impact model [10]. When a dynamical model is established using any of the aforementioned models, numerical simulations can then be conducted to demonstrate the behavior of the VI systems. Numerous studies have been conducted on systems with different degrees of freedom (DOFs) and parameters, and the general dynamical behavior of VI oscillators has revealed extremely rich response forms ranging from periodic to chaotic [11,12], as well as complicated bifurcations sensitive to system parameters [13–15].

Along with numerical findings, considerable effort has been made to study VI systems analytically. A widely accepted method to solve periodic responses of systems containing either bilinear or stereo-mechanical impacts is to represent the responses by Poincaré maps. These maps relate the states of the system at successive impacts by relying on the fact that the trajectories between impacts are linear and thus solvable. The equations can be used to construct return maps so that periodic steady-state responses can be solved. Since its early development [16], the method has been successfully applied to solve periodic responses involving a single impact per period [7,17], while Nigm et al. [18] extended its formulation to include more impacts per period by introducing impact distribution parameters. However, the equations assembled this way are typically nonlinear and require numerical methods to solve. This causes trouble when the number of impacts involved in each period increases and the equations become complicated, since it will be difficult to find available initial guesses from which the nonlinear solvers will converge.

The present work has two objectives. First, it aims at overcoming difficulties in solving the assembled equations for the periodic responses of VI systems by fitting them into a scheme of continuation that has been widely adopted in studies of nonlinear normal modes (NNMs), as defined in [19–21]. Previous research has shown that an efficient way to obtain NNMs is by continuation based on shooting methods that can be applied directly to the equations of motion (EOMs) or the approximate solutions of a system [9]. Several efforts have been made to solve the NNMs of VI systems. Using a nonsmooth temporal transform method developed in [22,23], Lee et al. [24] obtained the frequency-energy plot (FEP) of a 2-DOF VI system with stereo-mechanical impact model and studied its potentials in achieving targeted energy transfers. Moussi et al. [9] obtained the FEP of a 2-DOF VI system with bilinear model by first regularizing the nonsmooth terms in equations and then applying a combination of the harmonic balance method and the asymptotic numerical method. The present work serves as a complement to the existing studies by employing the return map equations to solve the exact NNMs and general periodic responses of a 2-DOF self-impacting oscillator with stereo-mechanical model. Similar work has been done by Thorin et al. [25], where periodic orbits involving one and two impacts per period are satisfactorily solved but numerical difficulties are met for more complicated cases. As an attempt to correct such difficulties, the present study points out that it is feasible to conduct piecewise continuation by treating periodic orbits involving different numbers of impacts separately, and starting each section by extracting available initial guesses out of grazing solution points where two or more different response forms intersect [26,27].

The second objective is to use the present method in performing a detailed examination of the FEP structures for both VI impacting systems and systems with odd-ordered polynomial internal forces. The method is efficient in that it is capable of detecting the existence of potential branches on FEP as much as one specifies. Moreover, by investigating critical points on the solution branches, the bifurcations on the FEP are analyzed in detail. The FEP of a system with an essential nonlinearity has been recognized as having a countable infinity of tongues [28], and the present study reveals that a major class of bifurcations on the FEP can be interpreted as cascades of period multiplying that are likely leading to pseudo-periodic or chaotic responses and the complete FEP grows in the form of infinite fractals. This observation suggests that a major family of general free responses, if not all, can be tracked along such bifurcations from the elementary NNMs. Since limitations have been known for the superposition of NNMs [29,30], such bifurcations can be considered as a counterpart to the linear normal mode superpositions. Same conclusions are applicable to NNMs and general free responses of conservative systems with smooth nonlinearities appearing in polynomials as well, based on the fact that rigid impacts can be interpreted as an extreme case of polynomial nonlinearity [31]. The manuscript exhibits such similarities by explaining how features revealed in the VI system can find their counterparts on the FEP of polynomially nonlinear systems.

2 Methodology

Consider the 2-DOF self-impacting oscillator shown in Fig. 1a. Two masses m_1 and m_2 are coupled by a linear spring of stiffness k_2, while m_1 is connected to ground by another linear spring of stiffness k_1. The global displacements of the masses are denoted as u_1 and u_2, respectively, with origins defined at the equilibrium state when both springs are unstretched. During any motion of the system, impacts may happen between

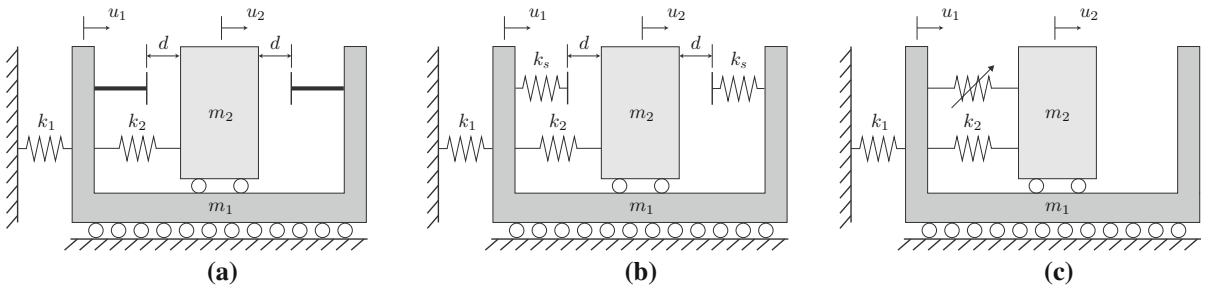

Fig. 1 System schematics: **a** VI system with stereo-mechanical model; **b** VI system with bilinear model; **c** linear oscillator with a nonlinear attachment (NES)

the masses as m_2 hits the rigid stops on m_1, which are of the same distance d away from the original position of m_2. The stereo-mechanical impact model is adopted: impacts are assumed instantaneous and are approximated by the introduction of a coefficient of restitution ε.

The periodic responses of this system are studied by piecewise continuation, where damping and external forcing is temporarily neglected to ensure the conservation of energy. The method can be regarded as a degenerate version of the discontinuous mapping scheme for general nonlinear VI systems [26].

2.1 Equations of motion

The EOMs for the unforced VI oscillator can be written as:

$$\begin{cases} m_1\ddot{u}_1 + (k_1+k_2)u_1 - k_2u_2 = 0 \\ m_2\ddot{u}_2 - k_2u_1 + k_2u_2 = 0 \end{cases}, \tag{1}$$

where impacts happen when $|u_2 - u_1| \geq d$. After each impact the velocities of the masses are updated, according to the conservation of momentum [15,32], by

$$\begin{aligned} \begin{bmatrix} \dot{u}_1^+ \\ \dot{u}_2^+ \end{bmatrix} &= \frac{1}{m_1+m_2} \begin{bmatrix} m_1 - m_2\varepsilon & m_2 + m_2\varepsilon \\ m_1 + m_1\varepsilon & m_2 - m_1\varepsilon \end{bmatrix} \begin{bmatrix} \dot{u}_1^- \\ \dot{u}_2^- \end{bmatrix} \\ &= \boldsymbol{G} \begin{bmatrix} \dot{u}_1^- \\ \dot{u}_2^- \end{bmatrix}, \end{aligned} \tag{2}$$

where the superscripts $-$ and $+$ represent the velocities before and after the impact, respectively, and ε is the coefficient of restitution with $0 \leq \varepsilon \leq 1$. To ensure conservation of energy, the impacts are assumed elastic during the analysis so that $\varepsilon = 1$.

It is convenient to introduce scaled displacements $x_i = u_i/d,\ i = 1, 2$ and the EOMs of the vibro-impact system (1) become

$$\begin{cases} m_1\ddot{x}_1 + (k_1+k_2)x_1 - k_2x_2 = 0 \\ m_2\ddot{x}_2 - k_2x_1 + k_2x_2 = 0 \end{cases}, \tag{3}$$

where impacts happen when $|x_2 - x_1| \geq 1$. Denote the scaled velocities as $y_i = \dot{x}_i,\ i = 1, 2$, so that they are updated after each impact by

$$\begin{bmatrix} \dot{y}_1^+ \\ \dot{y}_2^+ \end{bmatrix} = \boldsymbol{G} \begin{bmatrix} \dot{y}_1^- \\ \dot{y}_2^- \end{bmatrix}. \tag{4}$$

When $\varepsilon = 1$, the scaled energy is conserved and is simply

$$E_s = \frac{1}{2}\left[m_1y_1^2 + m_2y_2^2 + k_1x_1^2 + k_2(x_1 - x_2)^2\right]. \tag{5}$$

Since the energy of the physical system (1) before scaling is $E_p = d^2E_s$, the FEP under any clearance d can be obtained by stretching that of the scaled system (3), which is unique, along the energy axis by a factor of d^2.

2.2 Analogous systems

Before continuing the analysis, the potential significance of studying the system in (3) is illustrated by putting forward two comparable systems. First consider a vibro-impact oscillator represented by the bilinear model, which is very common in literature. As shown in Fig. 1b, instead of instantaneous impacts, the reaction force upon contact is approximated by a linear

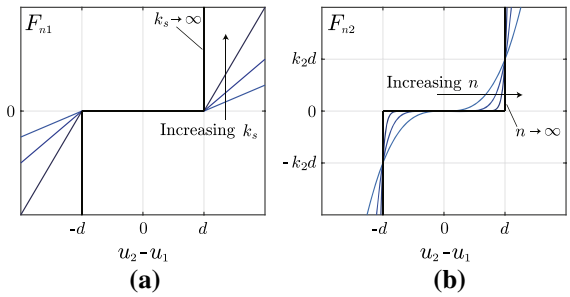

Fig. 2 Nonlinear internal forces: **a** bilinear vibro-impact system; **b** NES system

spring of stiffness k_s so that the equations of motion are

$$\begin{cases} m_1\ddot{u}_1 + (k_1+k_2)u_1 - k_2u_2 = F_{n1} \\ m_2\ddot{u}_2 - k_2u_1 + k_2u_2 = -F_{n1} \end{cases}, \tag{6}$$

where the piecewise reaction force F_{n1} is

$$F_{n1} = \begin{cases} k_s(u_2-u_1+d), & u_2-u_1 \le -d \\ 0, & |u_2-u_1| < d \\ k_s(u_2-u_1-d), & u_2-u_1 \ge d \end{cases}, \tag{7}$$

which is briefly plotted in Fig. 2a.

Next, consider the typical configuration of a nonlinear energy sink (NES) as shown in Fig. 1c, where the masses are coupled by an extra nonlinear spring. Without loss of generality the nonlinearity is assumed polynomial with odd-number powers, so that the EOMs can be written as:

$$\begin{cases} m_1\ddot{u}_1 + (k_1+k_2)u_1 - k_2u_2 = F_{n2} \\ m_2\ddot{u}_2 - k_2u_1 + k_2u_2 = -F_{n2} \end{cases}, \tag{8}$$

where the nonlinear force F_{n2} is formulated as

$$\begin{aligned} F_{n2} &= k_2 d\left(\frac{u_2-u_1}{d}\right)^n \\ &= \frac{k_2(u_2-u_1)^n}{d^{n-1}}, \quad n = 3, 5, 7, \ldots \end{aligned} \tag{9}$$

which is plotted in Fig. 2b. Instead of defining a nonlinear stiffness, a characteristic length d is introduced which is analogous to the clearance in the VI systems. According to Fig. 2, it is evident that $\lim_{k_s\to\infty} F_{n1} = \lim_{n\to\infty} F_{n2}$, so that the bilinear VI system (6) and the NES system (8) are equivalent at such extreme, and the characteristic length d approaches the physical clearance in the VI systems at the limit $n \to \infty$. [1] Shaw and Holmes [7] showed that the bilinear system (6) with $k_s \to \infty$ is equivalent to the stereo-mechanical-model system (1) with $\varepsilon \to 1$. Thus by comparing to the bilinear system, it can be concluded that the VI system (1), which is the focus of this work, is equivalent to the NES system (8) when $n \to \infty$ and $\varepsilon \to 1$. Similar conclusions have already been drawn in [31]. Furthermore, in Sect. 3.3, it is shown that similarities can be found between the NNMs of the VI system and those of the NES system with finite power n's, and that features of the VI system's FEPs have their counterparts in the FEPs of systems with polynomial nonlinearities.

The EOMs of the NES system (8) scaled by $x_i = u_i/d$ would become

$$\begin{cases} m_1\ddot{x}_1 + (k_1+k_2)x_1 - k_2x_2 = k_2(x_2-x_1)^n \\ m_2\ddot{x}_2 - k_2x_1 + k_2x_2 = -k_2(x_2-x_1)^n \end{cases}, \tag{10}$$

whose Hamiltonian is conserved and is expressed as

$$H_s = E_s + \frac{k_2}{n+1}(x_2-x_1)^{n+1}, \tag{11}$$

while the Hamiltonian of the original physical system (8) is

$$\begin{aligned} H_p &= E_p + \frac{k_2}{(n+1)d^{n-1}}(u_2-u_1)^{n+1} \\ &= d^2E_s + \frac{k_2d^{n+1}}{(n+1)d^{n-1}}(x_2-x_1)^{n+1} \\ &= d^2H_s \end{aligned}. \tag{12}$$

This shows that similar to the VI case, the FEP of any physical NES system (8) can be obtained by stretching that of the scaled system (10) along the energy axis by a factor of d^2. Notice by (9) that in essence either d or a conventionally defined nonlinear stiffness can solely represent the nonlinear internal force, one can always find the FEP of an NES system by expressing the nonlinear force in the form of (9) and only having to track the FEP of the scaled system (10). Generally, when the nonlinear force is expressed by a nonlinear stiffness such that

$$F_{n2} = k_c(u_2-u_1)^n = \frac{k_2(u_2-u_1)^n}{d^{n-1}}, \tag{13}$$

where k_c is the nonlinear stiffness, one can obtain the FEP under any k_c by first tracking the FEP of system (10) and stretching it by the factor $d^2 = (k_2/k_c)^{\frac{2}{n-1}}$, so that, for example, when $n = 3$, this stretching factor would be $d^2 = \frac{k_2}{k_c}$. The topologies of the FEP of a system with a single polynomial internal force, as in (8),

[1] Note that k_2 in the definition of F_{n2} (9) can actually be replaced by any fixed stiffness and the equivalence is still valid.

are totally determined by the linear system parameters and the order of the nonlinear force, while the nonlinear stiffness only determines the stretching along the energy (Hamiltonian) axis.

Systems in the form of (10) are considered fundamental in that it approaches the vibro-impact systems in Eqs. (3) and (4) when $n \to \infty$. Also since it is strictly constrained in the vibro-impact system that $|x_2 - x_1| \le 1$, the FEP of both systems are comparable in that $\lim_{n\to\infty} H_s = E_s$.

In the next section, the FEP of the vibro-impact system (3) is tracked by piecewise continuation based on mapping motion states at impacts, and is compared to the FEPs of system (10) with various n's obtained by continuation based on EOMs.

2.3 Continuation of periodic orbits

Instead of directly employing the EOMs, the NNMs and general periodic free responses of the VI system (3) are studied based on the Poincaré map from phases at an impact instant onto those at the next one, as developed in [7,16,18].

Consider a periodic free response that involves N impacts in one period T. Assume the impacts occur at time instants t_j, $j = 0, 1, \ldots, N$, where t_0 corresponds to the first impact, while t_N is the time instant of the first impact in the period that follows. First, the state vector can be written as $\boldsymbol{z}(t) = [x_1\ x_2\ y_1\ y_2]^{\mathrm{T}}$, and the states right after each impact are denoted as $\boldsymbol{z}_j$ which can be written as:

$$\boldsymbol{z}_j = \left[x_{1j}\ x_{2j}\ y_{1j}\ y_{2j}\right]^{\mathrm{T}} \triangleq \left[x_1\ x_2\ y_1^+\ y_2^+\right]^{\mathrm{T}}\Big|_{t=t_j} \tag{14}$$

and periodicity implies that $\boldsymbol{z}_N = \boldsymbol{z}_0$ and $t_N = t_0 + T$. Following [18], introduce N impact distribution parameters $\beta_k, k = 1, 2, \ldots, N$ so that the travel time between any pair of neighboring impacts is $\tau_k = t_k - t_{k-1} = \beta_k T$.

Since the system is linear between impacts, it can be solved using a linear modal analysis. Briefly, the natural frequencies of the linear system in (3) are

$$\omega_{1,2} = \sqrt{\frac{k_2}{2m_2} + \frac{k_1+k_2}{2m_1} \pm \Delta}\ , \tag{15}$$

where $\Delta = \sqrt{\frac{1}{4}\left(\frac{k_1+k_2}{m_1} + \frac{k_2}{m_2}\right)^2 - \frac{k_1 k_2}{m_1 m_2}}$, and $\omega_1 < \omega_2$. Then, the mass-normalized mode shapes $\boldsymbol{X}_1$ and $\boldsymbol{X}_2$ are assembled into matrix

$$\boldsymbol{\Phi} = [\boldsymbol{X}_1\ \boldsymbol{X}_2] = \begin{bmatrix} \frac{a_1}{\sqrt{m_1 a_1^2 + m_2}} & \frac{a_2}{\sqrt{m_1 a_2^2 + m_2}} \\ \frac{1}{\sqrt{m_1 a_1^2 + m_2}} & \frac{1}{\sqrt{m_1 a_2^2 + m_2}} \end{bmatrix}, \tag{16}$$

where $a_i = 1 - \dfrac{m_2\omega_i^2}{k_2}$. Also denote $\boldsymbol{\Psi} = \boldsymbol{\Phi}^{-1}$ so that the system can be written in principal coordinates $\boldsymbol{q} = \boldsymbol{\Psi}\boldsymbol{x}$. Moreover, denote vector $\hat{\boldsymbol{z}}(t) = [q_1\ q_2\ \dot{q}_1\ \dot{q}_2]^{\mathrm{T}}$ and extended matrices

$$\tilde{\boldsymbol{\Phi}} = \begin{bmatrix} \boldsymbol{\Phi} & \boldsymbol{0} \\ \boldsymbol{0} & \boldsymbol{\Phi} \end{bmatrix},\ \tilde{\boldsymbol{\Psi}} = \begin{bmatrix} \boldsymbol{\Psi} & \boldsymbol{0} \\ \boldsymbol{0} & \boldsymbol{\Psi} \end{bmatrix} \text{ and } \tilde{\boldsymbol{G}} = \begin{bmatrix} \boldsymbol{I}_{2\times 2} & \boldsymbol{0} \\ \boldsymbol{0} & \boldsymbol{G} \end{bmatrix}, \tag{17}$$

so that $\hat{\boldsymbol{z}}(t) = \tilde{\boldsymbol{\Psi}}\boldsymbol{z}(t)$, $\boldsymbol{z}(t) = \tilde{\boldsymbol{\Phi}}\hat{\boldsymbol{z}}(t)$ and particularly at impacts there is $\boldsymbol{z}_k = \tilde{\boldsymbol{G}}\tilde{\boldsymbol{\Phi}}\hat{\boldsymbol{z}}^-(t_k)$.

Consider the system's response in time interval $t \in [t_{k-1},\ t_k]$. The linear solution is simply

$$\begin{cases} q_i(t) = A_i \sin\omega_i(t - t_{k-1}) + B_i \cos\omega_i(t - t_{k-1}) \\ \dot{q}_i(t) = \omega_i A_i \cos\omega_i(t - t_{k-1}) - \omega_i B_i \sin\omega_i(t - t_{k-1}) \end{cases}, \tag{18}$$

whose coefficients are determined by initial conditions $\boldsymbol{z}_{k-1}$ as

$$[A_1\ A_2\ B_1\ B_2]^{\mathrm{T}} = \tilde{\boldsymbol{C}}\tilde{\boldsymbol{\Psi}}\boldsymbol{z}_{k-1}\ , \tag{19}$$

where the constant matrix $\tilde{\boldsymbol{C}}$ is

$$\tilde{\boldsymbol{C}} = \begin{bmatrix} \boldsymbol{0} & \boldsymbol{C} \\ \boldsymbol{I}_{2\times 2} & \boldsymbol{0} \end{bmatrix},\quad \boldsymbol{C} = \begin{bmatrix} 1/\omega_1 & 0 \\ 0 & 1/\omega_2 \end{bmatrix}. \tag{20}$$

Thus, at $t = t_k$, there is

$$\boldsymbol{z}_k = \boldsymbol{H}(\tau_k)\boldsymbol{z}_{k-1} \triangleq \left[\tilde{\boldsymbol{G}}\tilde{\boldsymbol{\Phi}}\tilde{\boldsymbol{H}}(\tau_k)\tilde{\boldsymbol{C}}\tilde{\boldsymbol{\Psi}}\right]\boldsymbol{z}_{k-1}\ , \tag{21}$$

where the matrix-valued function $\tilde{\boldsymbol{H}}(\tau)$ is defined as

$$\tilde{\boldsymbol{H}}(\tau) = \begin{bmatrix} s_1 & 0 & c_1 & 0 \\ 0 & s_2 & 0 & c_2 \\ \omega_1 c_1 & 0 & -\omega_1 s_1 & 0 \\ 0 & \omega_2 c_2 & 0 & -\omega_2 s_2 \end{bmatrix}, \tag{22}$$

with shorthands $s_i = \sin\omega_i\tau$ and $c_i = \cos\omega_i\tau$, $i = 1, 2$. Also in the following the notation $\boldsymbol{H}_k \triangleq \boldsymbol{H}(\tau_k) = \boldsymbol{H}(\beta_k T)$ is used.

Equation (21) gives the desired map so that $\boldsymbol{z}_k = \prod_{j=k}^{1} \boldsymbol{H}_j \boldsymbol{z}_0$ and thus $\boldsymbol{z}_N = \prod_{j=N}^{1} \boldsymbol{H}_j \boldsymbol{z}_0$, where the notation of product is reversed simply to emphasize the

order of matrix multiplications. At this point, the problem of solving a particular N-impact periodic response can be formulated explicitly as follows. The variables of the problem are taken as:

$$\boldsymbol{s} = \left[s_1\ s_2\ \ldots\ s_{N+5}\right]^{\mathrm{T}} = \left[\boldsymbol{z}_0^T\ \ \tilde{\boldsymbol{\beta}}^T\ \ T\right]^{\mathrm{T}}, \tag{23}$$

where $\tilde{\boldsymbol{\beta}} = [\beta_1\ \beta_2\ \ldots\ \beta_N]^{\mathrm{T}}$. Then, the problem is equivalent to solving the equations

$$\boldsymbol{F}(\boldsymbol{s}) = \left[\boldsymbol{F}_z^T\ \ \boldsymbol{F}_d^T\ \ f_b\right]^{\mathrm{T}} = \boldsymbol{0}, \tag{24}$$

where $\boldsymbol{F}_z$ lists the conditions for periodicity so that

$$\boldsymbol{F}_z = \boldsymbol{z}_N - \boldsymbol{z}_0 = \left(\prod_{j=N}^{1} \boldsymbol{H}_j - \boldsymbol{I}_{4\times 4}\right)\boldsymbol{z}_0, \tag{25}$$

and $\boldsymbol{F}_d = [f_{d1}\ \ f_{d2}\ \ \ldots\ \ f_{dN}]^{\mathrm{T}}$ enforces the condition of impact at time instants $t_0,\ t_1,\ \ldots,\ t_{N-1}$ so that

$$\begin{cases} f_{d1} = \boldsymbol{\Lambda}\boldsymbol{z}_0 + r_1, \\ f_{dn} = \boldsymbol{\Lambda}\boldsymbol{z}_{n-1} + r_n = \boldsymbol{\Lambda}\displaystyle\prod_{j=n-1}^{1} \boldsymbol{H}_j\boldsymbol{z}_0 + r_n,\ \ n \geq 2 \end{cases} \tag{26}$$

where $\boldsymbol{\Lambda} = [1\ \ -1\ 0\ 0]$, and $r_n = \pm 1$ defines the side on which the $(n-1)$th impact happens so that in practice the form of a response is characterized by both the number of impacts N and an array $\tilde{\boldsymbol{r}} = [r_1\ r_2\ \ldots\ r_N]$ specifying the locations of these impacts. Moreover, the function f_b implies that the sum of all β_k's is one, so that

$$f_b = \sum_{k=1}^{N} \beta_k - 1. \tag{27}$$

Notice that there are in total $N + 5$ elements in $\boldsymbol{F}(\boldsymbol{s})$ along with $N+5$ elements in $\boldsymbol{s}$, which seemingly implies that the problem is determinate so that the solutions should appear as points in the space $\mathbb{R}^{N+5}$. Yet, as shown later, the solutions form curves in the space, indicating that there is a redundant equation in (24). Given that the system is Hamiltonian, it is feasible to take any one element away from $\boldsymbol{F}_z$ and the solutions to the problem remain the same. However, this is not done here and $\boldsymbol{F}(\boldsymbol{s})$ is kept unchanged.

The problem can now be approached by the shooting method as follows. Given an initial guess $\boldsymbol{s}^{(0)}$, Newton's method is applied so that iterations proceed by

$$\boldsymbol{s}^{(i+1)} = \boldsymbol{s}^{(i)} + \boldsymbol{\zeta}, \quad \tilde{\boldsymbol{F}}'(\boldsymbol{s}^{(i)})\boldsymbol{\zeta} = -\tilde{\boldsymbol{F}}(\boldsymbol{s}^{(i)}), \tag{28}$$

where $\tilde{\boldsymbol{F}}(\boldsymbol{s}^{(i)}) = \begin{bmatrix} \boldsymbol{F}(\boldsymbol{s}^{(i)}) \\ 0 \end{bmatrix}$, and $\tilde{\boldsymbol{F}}'(\boldsymbol{s}^{(i)}) = \begin{bmatrix} \boldsymbol{J}(\boldsymbol{s}^{(i)}) \\ \boldsymbol{p}^T \end{bmatrix}$, where $\boldsymbol{J}(\boldsymbol{s})$ is the Jacobian matrix of $\boldsymbol{F}(\boldsymbol{s})$, which can be expressed as

$$\boldsymbol{J}(\boldsymbol{s}) = \frac{\partial \boldsymbol{F}}{\partial \boldsymbol{s}} = \begin{bmatrix} \dfrac{\partial \boldsymbol{F}_z}{\partial \boldsymbol{z}_0} & \dfrac{\partial \boldsymbol{F}_z}{\partial \tilde{\boldsymbol{\beta}}} & \dfrac{\partial \boldsymbol{F}_z}{\partial T} \\ \dfrac{\partial \boldsymbol{F}_d}{\partial \boldsymbol{z}_0} & \dfrac{\partial \boldsymbol{F}_d}{\partial \tilde{\boldsymbol{\beta}}} & \dfrac{\partial \boldsymbol{F}_d}{\partial T} \\ \dfrac{\partial f_b}{\partial \boldsymbol{z}_0} & \dfrac{\partial f_b}{\partial \tilde{\boldsymbol{\beta}}} & \dfrac{\partial f_b}{\partial T} \end{bmatrix}, \tag{29}$$

and $\boldsymbol{p}$ is a constant vector that is normal to the desired search direction, which is determined by the previous converged solution in continuation, as will be discussed later.

Although $\boldsymbol{J}(\boldsymbol{s})$ can be calculated symbolically, when N is large it is efficient to assemble it explicitly as follows.

Step 1 Partial derivatives that are easily obtained include

$$\frac{\partial \boldsymbol{F}_z}{\partial \boldsymbol{z}_0} = \prod_{j=N}^{1} \boldsymbol{H}_j - \boldsymbol{I}_{4\times 4}, \tag{30}$$

and

$$\frac{\partial f_{d1}}{\partial \boldsymbol{z}_0} = \boldsymbol{\Lambda}, \quad \frac{\partial f_{dn}}{\partial \boldsymbol{z}_0} = \boldsymbol{\Lambda}\prod_{j=n-1}^{1} \boldsymbol{H}_j, \quad n \geq 2, \tag{31}$$

and

$$\frac{\partial f_b}{\partial \boldsymbol{z}_0} = [0\ 0\ 0\ 0], \quad \frac{\partial f_b}{\partial \tilde{\boldsymbol{\beta}}} = [1\ 1\ \ldots\ 1]_{1\times N}, \quad \frac{\partial f_b}{\partial T} = 0. \tag{32}$$

Step 2 Denote

$$\boldsymbol{H}_j' = \frac{\partial \boldsymbol{H}_j}{\partial \tau_j} = \tilde{\boldsymbol{G}}\tilde{\boldsymbol{\Phi}}\frac{\partial \tilde{\boldsymbol{H}}(\tau_j)}{\partial \tau_j}\tilde{\boldsymbol{C}}\tilde{\boldsymbol{\Psi}}, \quad j = 1, 2, \ldots, N. \tag{33}$$

Then, $\dfrac{\partial \boldsymbol{F}_z}{\partial \tilde{\boldsymbol{\beta}}}$ can be evaluated by assembling

$$\frac{\partial \boldsymbol{F}_z}{\partial \beta_k} = \prod_{j=N}^{1} \boldsymbol{H}_{jk}^* \boldsymbol{z}_0, \quad \boldsymbol{H}_{jk}^* = \begin{cases} \boldsymbol{H}_j, & j \neq k \\ \boldsymbol{H}_j' T, & j = k \end{cases}, \tag{34}$$

and similarly $\dfrac{\partial \boldsymbol{F}_z}{\partial T}$ can be evaluated by

$$\frac{\partial \boldsymbol{F}_z}{\partial T} = \sum_{k=1}^{N}\prod_{j=N}^{1} \boldsymbol{H}_{jk}^\circ \boldsymbol{z}_0, \quad \boldsymbol{H}_{jk}^\circ = \begin{cases} \boldsymbol{H}_j, & j \neq k \\ \boldsymbol{H}_j' \beta_j, & j = k \end{cases}. \tag{35}$$

Step 3 Using the same notations, $\dfrac{\partial \boldsymbol{F}_d}{\partial \tilde{\boldsymbol{\beta}}}$ can be evaluated by assembling

$$\frac{\partial f_{dn}}{\partial \beta_k} = \begin{cases} \boldsymbol{\Lambda} \prod_{j=n-1}^{1} \boldsymbol{H}_{jk}^{*} \boldsymbol{z}_0, \ k \le n-1 \\ 0, \qquad\qquad k > n-1 \end{cases}, \tag{36}$$

and similarly, $\dfrac{\partial \boldsymbol{F}_d}{\partial T}$ can be evaluated as

$$\frac{\partial f_{dn}}{\partial T} = \begin{cases} \sum_{k=1}^{n-1} \boldsymbol{\Lambda} \prod_{j=n-1}^{1} \boldsymbol{H}_{jk}^{\circ} \boldsymbol{z}_0, \ n > 2 \\ 0, \qquad\qquad n = 1 \end{cases}. \tag{37}$$

With the scheme of shooting method established above, the curves in space $\mathbb{R}^{N+5}$ composed of solutions to the periodic responses are tracked by pseudo-arc-length continuation as in [33,34]. Briefly, denote $\boldsymbol{s}_j^{(i)}$ as the ith iteration in search of the jth solution point and $\boldsymbol{s}_j^{*}$ as the converged jth solution point. Then, the initial guess for the $(j+1)$th point is given by $\boldsymbol{s}_{j+1}^{(0)} = \boldsymbol{s}_j^{*} + \alpha \boldsymbol{p}_j$, where α is a predefined step length and $\boldsymbol{p}_j$, which is the tangent vector at $\boldsymbol{s}_j^{*}$, lies in the null space of $\boldsymbol{J}(\boldsymbol{s}_j^{*})$, and $\boldsymbol{p}_j$ is assigned as the normal direction vector in $\tilde{\boldsymbol{F}}'(\boldsymbol{s}_{j+1}^{(i)})$ for all iterations $\boldsymbol{s}_{j+1}^{(i)}$.

It needs to be reiterated that the method developed above deals with different forms of responses separately, which are classified by both the number of impacts N and the predefined locations of the impacts. Thus, in the following, a solution form is described as $A_N[R]$, where R is an N-bit binary series defining the impact locations. Denote impacts at side $x_2 - x_1 = 1$ as '0' and impacts at side $x_1 - x_2 = 1$ as '1'. Then, for example, $A_4[0101]$ refers to the responses that have 4 impacts per period, where the 1st and 3rd impacts happen at side $x_2 - x_1 = 1$, while the 2nd and 4th impacts happen at side $x_1 - x_2 = 1$.

Notice that the letter 'A' in the above notation indicates the asymmetric nature of the solution that the impacts in each period can be distributed arbitrarily. Yet in fact, as will be demonstrated, a major subset of solutions satisfy the symmetric condition $\boldsymbol{z}(t+T/2) = -\boldsymbol{z}(t)$. In the following, a symmetric response form is denoted as $S_N[R]$, similar to the definition of a general asymmetric solution. It is clear that for a symmetric response form N must be even, and the second half of R is the binary negation of the first half.

Moreover, a response form $A_N[R]$ can have one or more equivalent forms. First, $A_N[R]$ is always equivalent to $A_N[\neg R]$, where $\neg R$ is the binary negation of R, due to the symmetry of the clearances in the system configuration. Then since any R starting with '1' can always find its equivalent negation form starting with '0', in the following the first bit in R is assumed '0' for convenience. Meanwhile, $A_N[R]$ is also equivalent to all solution forms that appear as $A_N[R^{\rightarrow m}], m = 1, 2, \ldots, N-1$, where $R^{\rightarrow m}$ refers to R rotated by m bits forward. And finally, $A_N[R]$ is equivalent to $A_N[\neg R^{\rightarrow m}]$. Define two response forms as independent if they are not equivalent in any manner. Then, for example, Table 1 shows that there are only 2 independent forms $A_3[R_1]$ and $A_3[R_2]$ for $N = 3$.

Table 1 Possible response forms of $A_3[R]$

Notation	Binary series	Equivalent to
R_1	001	–
$R_1^{\rightarrow 1}$	100	R_1
$R_1^{\rightarrow 2}$	010	R_1
$\neg R_1$	110	R_1
$\neg R_1^{\rightarrow 1}$	011	R_1
$\neg R_1^{\rightarrow 2}$	101	R_1
R_2	000	–
$\neg R_2$	111	R_2

Furthermore, denote $P(N)$ as the number of possible independent forms of R for a given number of impacts N, and according to Pólya enumeration theorem [35], an estimation of $P(N)$ can be given by:

$$\hat{P}(N) = \frac{1}{2}\left[\frac{1}{N}\sum_{j|N} \varphi(j) 2^{N/j} + \hat{p}\,(N/2)\right], \tag{38}$$

where $j|N$ states that j is a positive integer divisor of N, $\varphi(j)$ is Euler's totient function that counts the positive integers up to j that are coprime with j, and $\hat{p}(N/2)$ counts the number of positive integer divisors of $N/2$ when N is even and $\hat{p}(N/2) = 0$ when N is odd. It turns out that $\hat{P}(N) = P(N)$ when N is odd, but $\hat{P}(N)$ is a lower bound of $P(N)$ when N is even.

2.4 Details of implementation

2.4.1 Admissibility of solutions

It should be noted that the method assumes linear flight between time instants of impact, which may be violated

in many solutions. When a solution is given, the linear response between each pair of neighboring impacts is tested to see whether the condition $|x_2 - x_1| \geq 1$ is met at any time instant, and if so the solution is tagged as inadmissible.

Inadmissible solutions do not exist physically and are just redundant mathematical solutions to the equations. However, the transition points at which a branch of solution turns from admissible to inadmissible are critically useful for the method to work. Note that since the continuation is done piecewise, a feasible initial guess is required each time a new branch $A_N[R]$ is to be tracked, this becomes computationally inefficient as N gets large. To overcome this, the following shows that a reasonable starting point can be achieved by estimating the initial guesses from the admissibility transition points of previously solved branches.

Suppose at a transition point the solution involves N regular impacts (where the masses touch with nonzero relative velocity) while meeting the condition $|x_2 - x_1| = 1$ at p time instants where grazing occurs so that the masses touch with zero relative velocity. Such a point with N regular impacts and p grazing instants is the end of branch $A_N[R]$, and it is anticipated that another branch $A_{N+p}[R']$ also ends (or starts) at the same point, where R' is the new $(N+p)$-bit binary array with the sides on which the grazings occur are inserted into R. Suppose one tracks $A_N[R]$ till this transition point and wants to shift to the $A_{N+p}[R']$ branch. This can be done by inheriting the same z_0 and T while obtaining the new $N+p$ impact distribution parameter β's from the previous solution of $A_N[R]$ at the transition point, thereby forming the initial guess for the new branch $A_{N+p}[R']$. Similarly, if one tracks the $A_{N+p}[R']$ branch first, a feasible initial guess for $A_N[R]$ can be extracted by releasing the conditions for impacts at the p grazing instants.

In the following, such admissibility switching points are called as grazing solution points. Moreover, it will be shown later that there may be more than two branches coming out of a same grazing solution point since one can loose the impact condition for any one of the p grazing instants and obtain a new response form. Theoretically, a grazing solution point with p grazing instants can be the intersection of at most 2^p branches of different solution forms.

2.4.2 Stability of solutions

A solution that passes the admissibility test is regarded as an existing periodic orbit of the system and will appear on the FEP. However, an admissible solution can be unstable so that any perturbation will lead the system response to other forms. The stability of the solutions are examined as follows.

Given an admissible solution $\boldsymbol{s} = \left[\boldsymbol{z}_0^T \;\; \tilde{\boldsymbol{\beta}}^T \;\; T\right]^{\mathrm{T}}$, the values of z_k and $\tau_k = t_k - t_{k-1}$, $k = 1, 2, \ldots, N$, can be extracted. Next, construct the Poincoré map of variables $\boldsymbol{v}_j = \left[\boldsymbol{z}_j^T \;\; t_j\right]^{\mathrm{T}}$, $j = 0, 1, \ldots, N$, then the stability of the given solution is determined by the eigenvalues of the Jacobian matrix of a return map

$$\boldsymbol{v}_N^P = \left[\boldsymbol{z}_N^T \;\; t_N - T\right]^{\mathrm{T}} = \boldsymbol{F}_r(\boldsymbol{v}_0) = \boldsymbol{v}_0, \tag{39}$$

where the superscript 'P' refers to the subtraction of period T from t_N. Thus, the desired Jacobian matrix is

$$\boldsymbol{J}_{N,0} = \frac{\mathrm{d}\boldsymbol{v}_N^P}{\mathrm{d}\boldsymbol{v}_0} = \frac{\mathrm{d}\boldsymbol{v}_N}{\mathrm{d}\boldsymbol{v}_0} = \prod_{k=N}^{1} \boldsymbol{J}_{k,k-1}, \tag{40}$$

where

$$\boldsymbol{J}_{k,k-1} = \frac{\mathrm{d}\boldsymbol{v}_k}{\mathrm{d}\boldsymbol{v}_{k-1}} = \begin{bmatrix} \dfrac{\mathrm{d}z_k}{\mathrm{d}z_{k-1}} & \dfrac{\mathrm{d}z_k}{\mathrm{d}t_{k-1}} \\ \dfrac{\mathrm{d}t_k}{\mathrm{d}z_{k-1}} & \dfrac{\mathrm{d}t_k}{\mathrm{d}t_{k-1}} \end{bmatrix}. \tag{41}$$

Recall that $z_k = \boldsymbol{H}_k z_{k-1}$ and $\boldsymbol{H}_k' = \dfrac{\partial \boldsymbol{H}_k}{\partial \tau_k} = \dfrac{\partial \boldsymbol{H}_k}{\partial t_k} = -\dfrac{\partial \boldsymbol{H}_k}{\partial t_{k-1}}$, by taking the derivatives of the implicit equation $\boldsymbol{\Lambda} z_k = \pm 1$, there are

$$\begin{aligned} \frac{\mathrm{d}\boldsymbol{\Lambda} z_k}{\mathrm{d}z_{k-1}} &= \frac{\mathrm{d}\boldsymbol{\Lambda}\boldsymbol{H}_k z_{k-1}}{\mathrm{d}z_{k-1}} \\ &= \frac{\partial \boldsymbol{\Lambda}\boldsymbol{H}_k z_{k-1}}{\partial t_k}\frac{\mathrm{d}t_k}{\mathrm{d}z_{k-1}} + \boldsymbol{\Lambda}\boldsymbol{H}_k \\ &= \boldsymbol{\Lambda}\boldsymbol{H}_k' z_{k-1}\frac{\mathrm{d}t_k}{\mathrm{d}z_{k-1}} + \boldsymbol{\Lambda}\boldsymbol{H}_k = \boldsymbol{0}, \end{aligned} \tag{42}$$

and

$$\begin{aligned} \frac{\mathrm{d}\boldsymbol{\Lambda} z_k}{\mathrm{d}t_{k-1}} &= \frac{\mathrm{d}\boldsymbol{\Lambda}\boldsymbol{H}_k z_{k-1}}{\mathrm{d}t_{k-1}} \\ &= \frac{\partial \boldsymbol{\Lambda}\boldsymbol{H}_k z_{k-1}}{\partial t_k}\frac{\mathrm{d}t_k}{\mathrm{d}t_{k-1}} + \frac{\partial \boldsymbol{\Lambda}\boldsymbol{H}_k z_{k-1}}{\partial t_{k-1}} \\ &= \boldsymbol{\Lambda}\boldsymbol{H}_k' z_{k-1}\left(\frac{\mathrm{d}t_k}{\mathrm{d}t_{k-1}} - 1\right) = 0, \end{aligned} \tag{43}$$

yielding

$$\frac{\mathrm{d}t_k}{\mathrm{d}z_{k-1}} = -\frac{\boldsymbol{\Lambda}\boldsymbol{H}_k}{\boldsymbol{\Lambda}\boldsymbol{H}_k' z_{k-1}}, \quad \text{and} \quad \frac{\mathrm{d}t_k}{\mathrm{d}t_{k-1}} = 1, \tag{44}$$

giving the bottom row of $\boldsymbol{J}_{k,k-1}$, while the rest are then calculated by

$$\frac{\mathrm{d}\boldsymbol{z}_k}{\mathrm{d}\boldsymbol{z}_{k-1}} = \boldsymbol{H}'_k \boldsymbol{z}_{k-1} \frac{\mathrm{d}t_k}{\mathrm{d}\boldsymbol{z}_{k-1}} + \boldsymbol{H}_k, \tag{45}$$

and

$$\begin{aligned} \frac{\mathrm{d}\boldsymbol{z}_k}{\mathrm{d}t_{k-1}} &= \frac{\partial \boldsymbol{H}_k \boldsymbol{z}_{k-1}}{\partial t_k} \frac{\mathrm{d}t_k}{\mathrm{d}t_{k-1}} + \frac{\partial \boldsymbol{H}_k \boldsymbol{z}_{k-1}}{\partial t_{k-1}} \\ &= \boldsymbol{H}'_{\boldsymbol{k}} \boldsymbol{z}_{k-1}(1-1) = \boldsymbol{0}. \end{aligned} \tag{46}$$

A solution is stable if all the eigenvalues of the Jacobian matrix $\boldsymbol{J}_{N,0}$, i.e., the Floquet multipliers, lie inside the unit circle on the complex plane. However, $\boldsymbol{J}_{N,0}$ always has an eigenvalue at 1, so that all the stable solutions are in fact marginally stable, which means that the system's response under initial conditions in the neighborhood of $\boldsymbol{z}_0$ will not be attracted to the solved periodic orbit, but instead appear in a pseudo-periodic form. This is analogous to the case of linear normal modes.

2.4.3 Critical points

Recall that when a solution point $\boldsymbol{s}_j^*$ for a response form $A_N[R]$ is obtained, the tangent vector $\boldsymbol{p}_j$ of the solution curve at this point in the $\mathbb{R}^{N+5}$ space lies in the null space of matrix $\boldsymbol{J}(\boldsymbol{s}_j^*)$. Normally, the dimension of such null space is 1, so that $\boldsymbol{J}(\boldsymbol{s}_j^*)$ has a unique eigenvalue at 0 and $\boldsymbol{p}_j$ is simply the corresponding eigenvector. However, during continuation critical points have been observed, where $\boldsymbol{J}(\boldsymbol{s}_j^*)$ has more than one zero eigenvalue, so that the dimension of the null space may become greater than 1 and instead of being the tangent vector, the corresponding eigenvectors can only give a basis for potential tangent vectors. Denote the algebraic multiplicity of the zero eigenvalue $\lambda = 0$ as a and its geometric multiplicity as b, by which the critical points that have been observed can be categorized below.

Case 1 $a = 2$ or 3, $b = 1$. The tangent vector is still directly given by the repeating eigenvector so that there are no bifurcations, but typically the stability of the solutions changes at such critical points, corresponding to a saddle-node bifurcation.

Case 2 $a = 2$ or 3, $b = 2$. The solution curve bifurcates into two branches, typically corresponding to a pitchfork bifurcation.

Case 3 $a = 3$, $b = 3$. The solution curve bifurcates into four branches, whose tangent vectors cannot be directly obtained. In such case, the method developed in [36] is applied to solve for the four available tangent directions, which involves the evaluation of the Hessian matrices for all functions in $\boldsymbol{F}(\boldsymbol{s})$.

3 Results

3.1 Elementary structure of FEP

In this section, the frequency-energy plot of the vibro-impact system is generated piecewise by the continuation method developed above, where the scaled energy E_s of admissible solutions are plotted against the angular velocity corresponding to their shortest period. Note that a solution in the form $A_N[R]$ with period T can also be extended to satisfy the equations for the response form $A_{kN}[R^k]$ with period kT, where k is any positive integer and R^k is R repeated k times. However, it should only appear on the FEP as $A_N[R]$ with frequency $\omega = \frac{2\pi}{T}$. For example, if $\boldsymbol{s}_1 = \left[\boldsymbol{z}_0^T \;\; \tilde{\boldsymbol{\beta}}^T \;\; T\right]^{\mathrm{T}}$ is a solution for $A_2[01]$, then $\boldsymbol{s}_2 = \left[\boldsymbol{z}_0^T \;\; \frac{\tilde{\boldsymbol{\beta}}^T}{2} \;\; \frac{\tilde{\boldsymbol{\beta}}^T}{2} \;\; 2T\right]^{\mathrm{T}}$ is a solution for $A_4[0101]$ and $\boldsymbol{s}_3 = \left[\boldsymbol{z}_0^T \;\; \frac{\tilde{\boldsymbol{\beta}}^T}{3} \;\; \frac{\tilde{\boldsymbol{\beta}}^T}{3} \;\; \frac{\tilde{\boldsymbol{\beta}}^T}{3} \;\; 3T\right]^{\mathrm{T}}$ will be a solution for $A_6[010101]$, etc. The 3 solutions $\boldsymbol{s}_1$, $\boldsymbol{s}_2$ and $\boldsymbol{s}_3$ will correspond to three points on the FEP with identical energy but $\frac{2\pi}{T}$, $\frac{\pi}{T}$ and $\frac{2\pi}{3T}$ as frequencies. Note that the latter two points are invalid because $2T$ and $3T$ are not their shortest periods. In what follows, a branch that is a k-time repeating form of $A_N[R]$ is called its k-duplicate and is notated as $A_N^k[R]$, while $A_N[R]$ which is not a lower-frequency duplicate of any other branch, and thus is plotted right at the shortest periods, is called an original branch. On the FEP, duplicate branches will be shown in dashed lines and they are in fact the corresponding original $A_N[R]$ branches shrunk by a factor of $\frac{1}{k}$ along the frequency axis.

The FEP is demonstrated step by step so that the previously mentioned details of the method can be clarified. Referring to Eq. (3), the system parameters adopted are

$$m_1 = 2,\; m_2 = 2\,\mathrm{kg},\; k_1 = 8k_2 = 8\,\mathrm{N/m},\; \varepsilon = 1. \tag{47}$$

Meanwhile, several notations are used in the plots. First, a critical point is notated as C_{ab}^i, where a and b are the algebraic and geometric multiplicities of the

zero eigenvalue of the Jacobian matrix, respectively, while i is simply its number in the C_{ab} family. (In fact $a = b = 1$ for all regular points on the curves.) Next, a grazing solution point is notated as $G^i_{N,p}$, where N is the number of regular impacts during one period and p is the number of grazing instants, and i is similarly its number in the $G_{N,p}$ family. Specifically, branches meeting at a bifurcating critical point should share the same response form $A_N[R]$, but may be different in symmetry, while branches meeting at a non-critical grazing solution point typically have different forms. Moreover, define a segment $A_N[R]|\underline{P_1 P_2}$ as the part of solution branch $A_N[R]$ bounded between points P_1 and P_2 on the FEP, where P_i $(i = 1, 2)$ is any defined point. Furthermore, three intrinsic frequencies are highlighted as reference for all FEPs shown below, including the natural frequencies of the 2-DOF linear system that are calculated under the chosen system parameters to be $\omega_1 = 0.9287$ rad/s and $\omega_2 = 2.1535$ rad/s, respectively, and a third frequency defined as

$$\omega_0 = \sqrt{\frac{k_1}{m_1 + m_2}} = 1.6330 \text{ rad/s}, \tag{48}$$

which is the natural frequency of a single-DOF system with parameters inherited from the original 2-DOF system, where m_2 is fixed on m_1 and connected to ground by the linear spring with stiffness k_1.

The initialization of continuation is shown in Fig. 3. At low energies, there exist only the linear normal modes involving no impacts, which can be denoted as A_0 or, by their symmetric nature, S_0. Particularly, denote S_0^+ as the in-phase mode corresponding to $\boldsymbol{X}_1$, and S_0^- as the out-of-phase mode corresponding to $\boldsymbol{X}_2$. These linear modes are admissible and stable until they reach the grazing solution points $G^1_{0,2}$ and $G^2_{0,2}$, respectively, the time histories of which are also given in Fig. 3. At either grazing solution point, 2 grazing instants appear simultaneously, indicating the potential existence of 2 independent solution branches: $A_1[0]$ and $A_2[01]$. However, all $A_1[0]$ solutions passing through these grazing solution points turned out inadmissible, so that only the $A_2[01]$ branches are observed. The initial guesses for the continuation of the $A_2[01]$ branches are obtained by first plugging in the motion states at the first grazing instant as $\boldsymbol{z}_0$, using the same time period T of the grazing solution, and finally reading the impact distribution parameters from the time history at the grazing solution points, which are, in

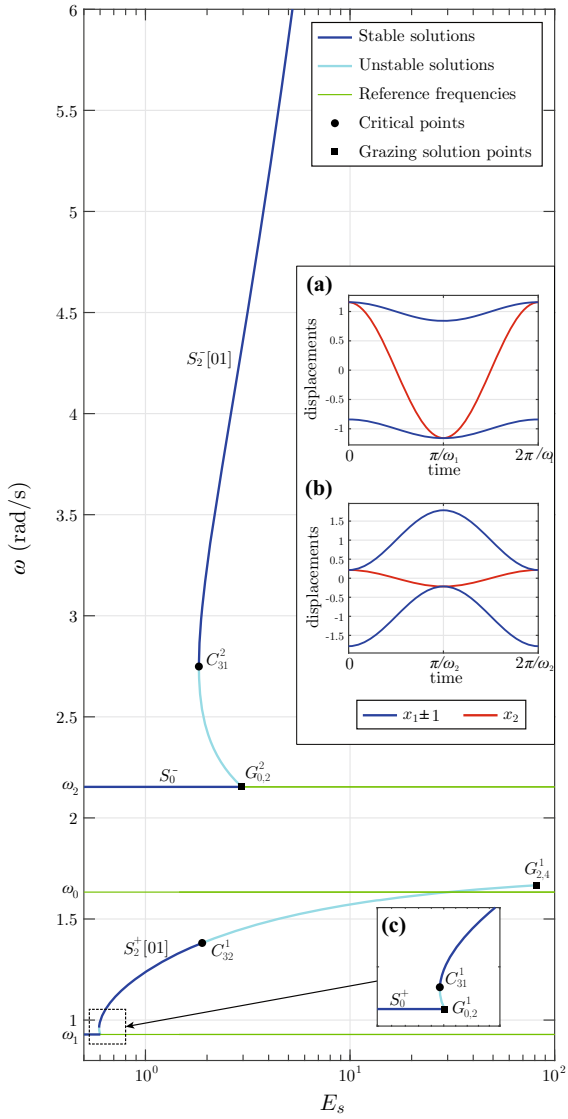

Fig. 3 FEP during the initialization of continuation, including transitions from linear normal modes S_0 to symmetric NNMs $S_2[01]$: **a** time history at $G^1_{0,2}$; **b** time history at $G^2_{0,2}$; **c** details around the transition of the in-phase modes

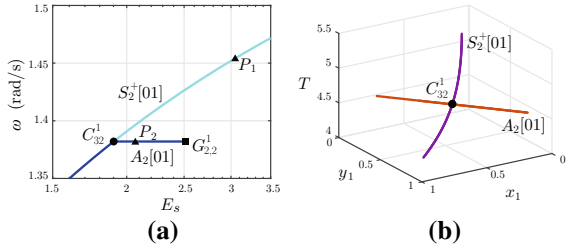

Fig. 4 Bifurcation at critical point C^1_{32}: **a** FEP; **b** projections of the solution curves

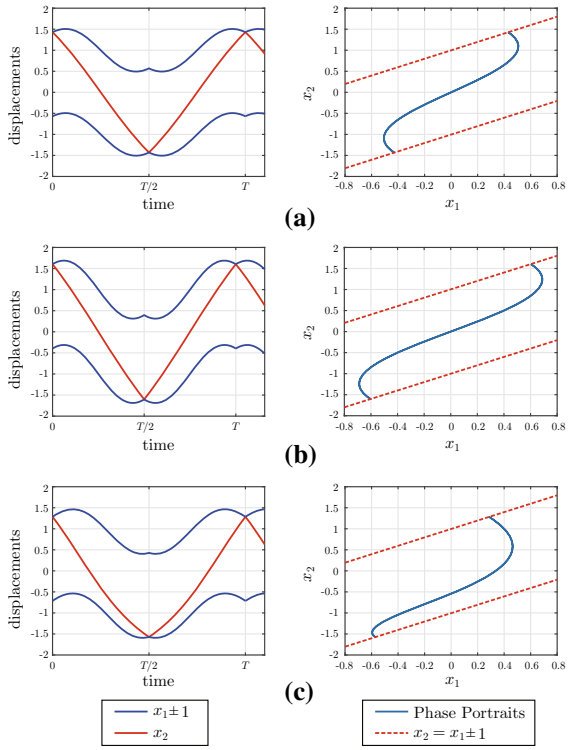

Fig. 5 Time histories and phase portraits at selected solution points on the FEP shown in Fig. 4a: **a** C_{32}^1; **b** regular point P_1; **c** regular point P_2

such case, $\beta_1 = \beta_2 = \frac{1}{2}$. The two $A_2[01]$ branches thus initiated have inherited the symmetric nature and can be correspondingly denoted as $S_2^+[01]$ and $S_2^-[01]$.

The $S_2^-[01]$ branch is unstable and decreasing in energy at the beginning until it hits the critical point C_{31}^2, which stands for a local minimum of energy, and then becomes stable while extending to infinite frequency and energy without meeting any critical or grazing solution points afterward. Similarly, the $S_2^+[01]$ branch turns stable after hitting the energy-minimizing critical point C_{31}^1. However, it becomes unstable again after hitting another critical point C_{32}^1, which indicates a potential bifurcation into 2 branches since the geometric multiplicity of the zero eigenvalue is 2. Moreover, instead of extending to infinity, the $S_2^+[01]$ branch meets the grazing solution point $G_{2,4}^1$ and turns inadmissible beyond it.

The bifurcating critical point C_{32}^1 is treated first. While one of the two independent eigenvectors gives the direction along $S_2^+[01]$, the other leads to another $A_2[01]$ branch where symmetry breaks down but stability is restored, as shown in Fig. 4a, which ends at the grazing solution point $G_{2,2}^1$. Meanwhile, Fig. 4b depicts the 2 solution curves in the neighborhood of C_{32}^1 as projections from $\mathbb{R}^7$ onto the subspace consisted of variables $[x_1 \ y_1 \ T]^{\mathrm{T}}$. It is interesting to observe that this new segment $A_2[01]|\overline{C_{32}^1 G_{2,2}^1}$ is horizontal on FEP so that it is frequency-invariant. Furthermore, the time histories and phase portraits of 2 randomly selected points P_1 and P_2 marked in Fig. 4 as well as those at C_{32}^1 are shown in Fig. 5 to illustrate the evolutions of the responses' shape around this critical point.

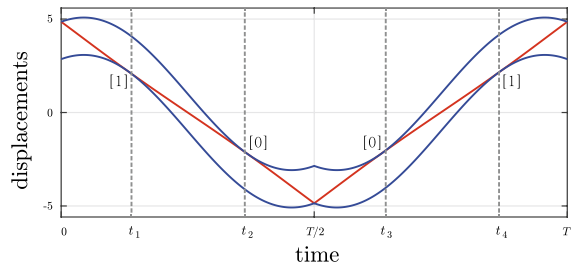

Fig. 6 Time history at grazing solution point $G_{2,4}^1$, with grazing instants and sides labeled on graph

Next, the typical grazing solution point $G_{2,4}^1$ at which $S_2^+[01]$ ends is studied in detail. The time history at this point is given in Fig. 6, where the 4 grazing instants are notated as t_i, $i = 1, 2, 3, 4$, respectively, and the binary notations of the grazing sides are labeled on graph. Particularly at this point, the $2^4 = 16$ possible branches can be denoted as binary series $[R_k] = [0r_1^k r_2^k 1 r_3^k r_4^k]$, where the variable r_i^k corresponds to the ith grazing instant, and can be either empty (denoted as '/') or the bit representing the grazing side as shown in Fig. 6. Due to the symmetry of the response, some of the 16 branches are equivalent and there are in total 7 independent possible solution forms:

$$\begin{cases} [R_1] = [0//1//] \rightarrow S_2^+[01] \\ [R_2] = [010101] \rightarrow A_6[010101]\,(S_6[010101]) \\ [R_3] = [0/0101] \rightarrow A_5[00101] \\ [R_4] = [0//10/] \rightarrow A_3[010] \\ [R_5] = [0//101] \rightarrow A_4[0101] \\ [R_6] = [0/01/1] \rightarrow A_4[0011]\,(S_4[0011]) \\ [R_7] = [0/010/] \rightarrow A_4[0010] \end{cases} \tag{49}$$

and continuation has to be carried out for each of them.

It turns out that all these 7 independent solution forms have their admissible branches setting out from

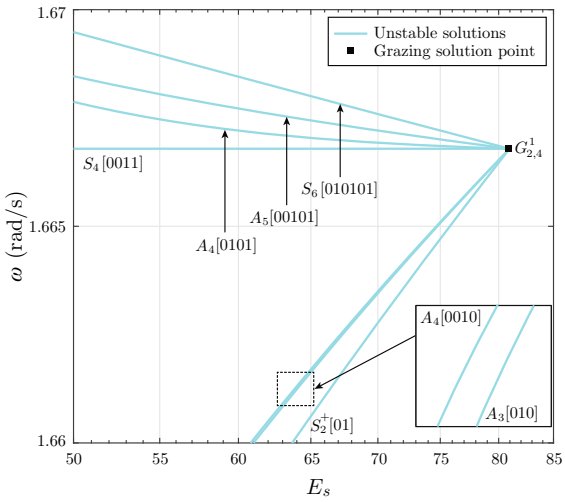

Fig. 7 Detailed FEP in the neighborhood of grazing solution point $G^1_{2,4}$

this grazing solution point, so that the FEP around $G^1_{2,4}$ is surprisingly complicated, as shown in Fig. 7. The other terminals of these branches are depicted in Fig. 8. Briefly, branches $A_3[010]$ and $A_4[0010]$ both end at the previously revealed grazing solution point $G^1_{2,2}$. Branches $A_4[0101]$ and $A_5[00101]$ end at $G^2_{4,2}$ and transit into a short segment $A_6[010101]|\underline{G^2_{4,2}C^3_{32}}$, which meets the $S_6[010101]$ branch at critical point C^3_{32}. It is also at this point that $S_6[010101]$ turns stable until hitting another critical point C^1_{33}, which should be the junction of 4 branches satisfying the form $A_6[010101]$. In fact, 3 of the 4 branches are identical on FEP, which are symmetric and extend to grazing solution point $G^1_{4,2}$, while the 4th branch is the 3-duplicate of $S^-_2[01]$ so that it is denoted as $S^{3-}_2[01]$ and shown in dashed line in Fig. 8. Finally, an $S_4[0011]$ branch starts from $G^1_{4,2}$ and changes stability at critical point C^2_{32} where it meets the frequency-invariant $S_4[0011]$ segment coming from $G^1_{2,4}$. The time histories at representative solution points are depicted in Fig. 9.

The above has revealed two significant issues regarding the completeness of an obtained FEP. First, grazing solution points can be the junction of surprisingly many solution branches that lead to different ends. Although the method is capable of tracking all possible forms, it will be very time consuming to conduct similar analysis for all grazing solution points as the continuation goes on with more and more impacts involved. Second, extra critical points can emerge on the duplicated branches, while they do not exist on the original branch, as in the case of $S^-_2[01]$ and its duplicate $S^{3-}_2[01]$ on which a critical point C^1_{33} appears. Since theoretically any branch that is already obtained can have infinitely many duplicates in the lower-frequency domain, it may be nearly impossible to predict the existence of all branches, let alone tracking them. Though, in what follows emphasis will be laid on uncovering the underlying patterns in the infinite FEP and it will be shown how the nature of the FEP can be related to fractals.

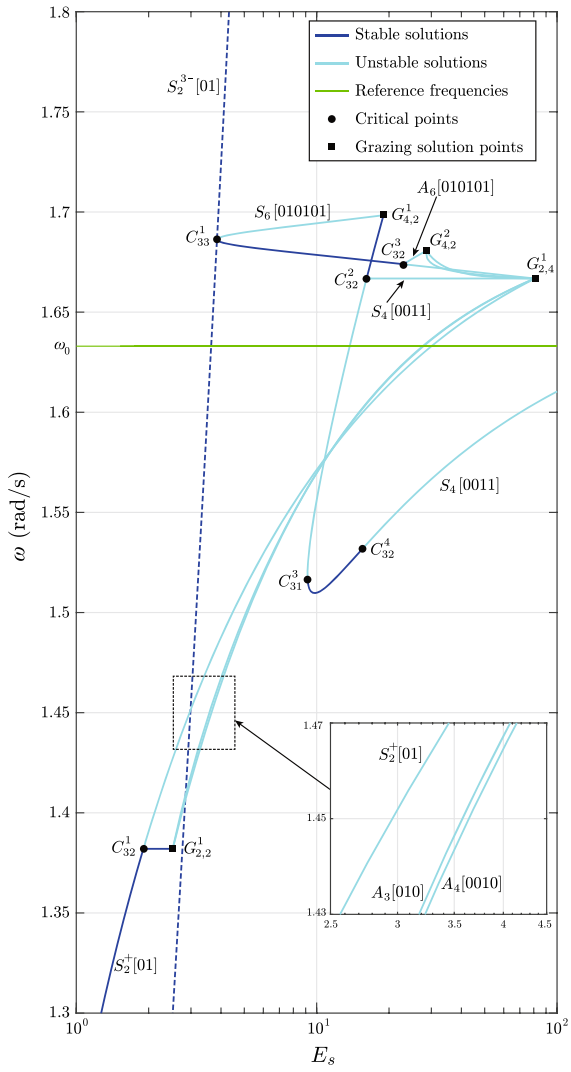

Fig. 8 FEP including full segments that end at $G^1_{2,4}$

Among all existing solution branches on the FEP, of most significance are those satisfying the condition

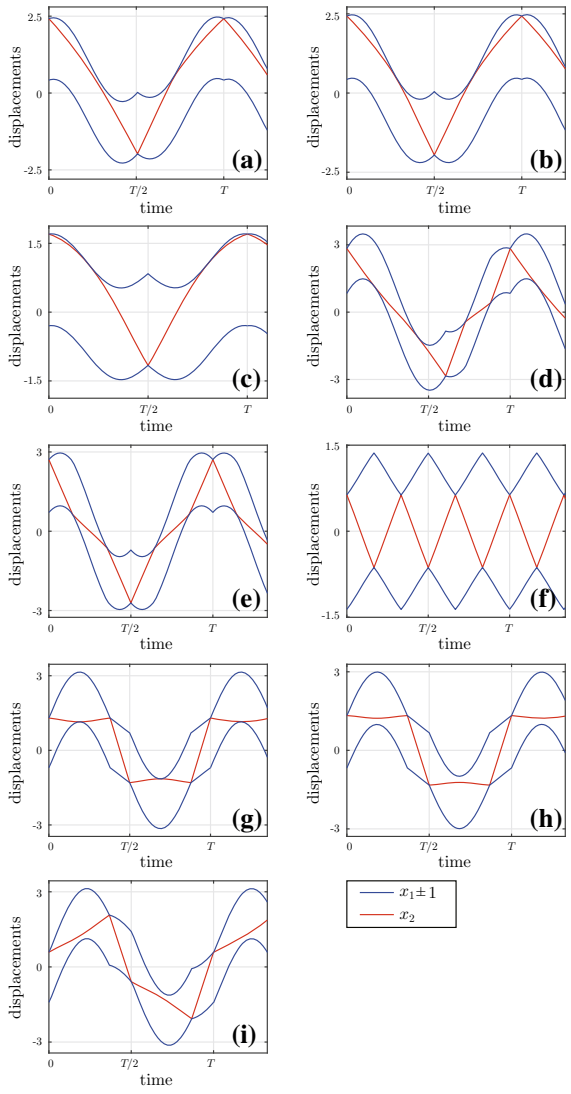

Fig. 9 Time histories at selected solution points on the FEP shown in Figs. 7 and 8: **a** Regular point on segment $A_3[010]|\underline{G^1_{2,4}G^1_{2,2}}$; **b** regular point on segment $A_4[0010]|\underline{G^1_{2,4}G^1_{2,2}}$; **c** $G^1_{2,2}$; **d** $G^2_{4,2}$; **e** C^3_{32}; **f** C^1_{33}; **g** $G^1_{4,2}$; **h** C^2_{32}; **i** regular point on segment $S_4[0011]|\underline{G^1_{2,4}C^2_{32}}$

of symmetry, including previously illustrated branches S_0, $S_2[01]$, $S_6[010101]$ as well as $S_4[0011]$. In fact, it is observed that the path connecting all the successive symmetric branches extending from the original S_0^+ linear branch represents the main body of the FEP within frequency range $[\omega_1\ \omega_2]$, which gradually approaches infinite energy while converging to ω_0 in frequency. Meanwhile, the asymmetric branches are either trivial deviations accompanying the major symmetric path, which is the case for the asymmetric branches starting from $G^1_{2,4}$, or continuous tongues that are localized in energy and frequency, which will be shown later. Picking up the continuation in Fig. 8 that paused at branch $S_4[0011]$, the path consisted of succeeding symmetric branches is depicted in Figs. 10 and 11 where labels and marks are omitted for the trivial branches and some of the critical/grazing solution points at high energy levels.

Two major families of branches are dominant in the symmetric path, while other trivial ones serve as connections among them. The first major family includes solutions in the form $S_{2k}[01]^k$, where $k \geq 3$ is an odd number and the superscript k stands for [01] repeated k times. Commonly, each $S_{2k}[01]^k$ branch intersects the duplicate branch $S_2^{k-}[01]$ at an energy-minimizing critical point in the C_{33} family. Meanwhile, there exists another C_{32} critical point on each of them and the branch is only stable on the segment between these two critical points. Furthermore, the ends of each $S_{2k}[01]^k$ branch are two grazing solution points, one of which is $G_{2k-2,2}$ and is at higher frequency, while the other one is $G_{2k-4,4}$ at lower frequency. The branches corresponding to $k = 3, 5, 7$ and 9 in this family have been shown in Figs. 10 and 11, and it is predicted that similar branches exist for $k > 9$. The second major family of solutions include those in the form $S_{2j}[0^j 1^j]$, where $j \geq 2$ is an integer and the superscripts j represent '0' and '1' repeated j times, respectively. Typically, an $S_{2j}[0^j 1^j]$ branch has 3 critical points where the first one is C_{32} at high frequency that can bifurcate into another symmetric side branch leading to a grazing solution point that is one end of the previous $S_{2(j-1)}[0^{j-1}1^{j-1}]$ branch, while the second one is C_{31} that only indicates a change of stability and the third one is another C_{32} that may bifurcate into asymmetric branches, which will be discussed later. The ends of such a branch are grazing solution points that are either the ends of an $S_{2k}[01]^k$ branch or a branch that extends from an $S_{2k}[01]^k$ branch. In other words, after all, by defining a common index $i \geq 3$ which is odd, the main body of the path of symmetric branches are constructed by successively connecting (directly or through short trivial symmetric branches) these 2 major families of branches in the order

$$S_{2i}[01]^i \rightarrow S_{i+1}[0^{\frac{i+1}{2}}1^{\frac{i+1}{2}}] \rightarrow S_{2(i+2)}[01]^{i+2} \rightarrow S_{i+3}[0^{\frac{i+3}{2}}1^{\frac{i+3}{2}}] \rightarrow S_{2(i+4)}[01]^{i+4} \rightarrow \ldots.$$

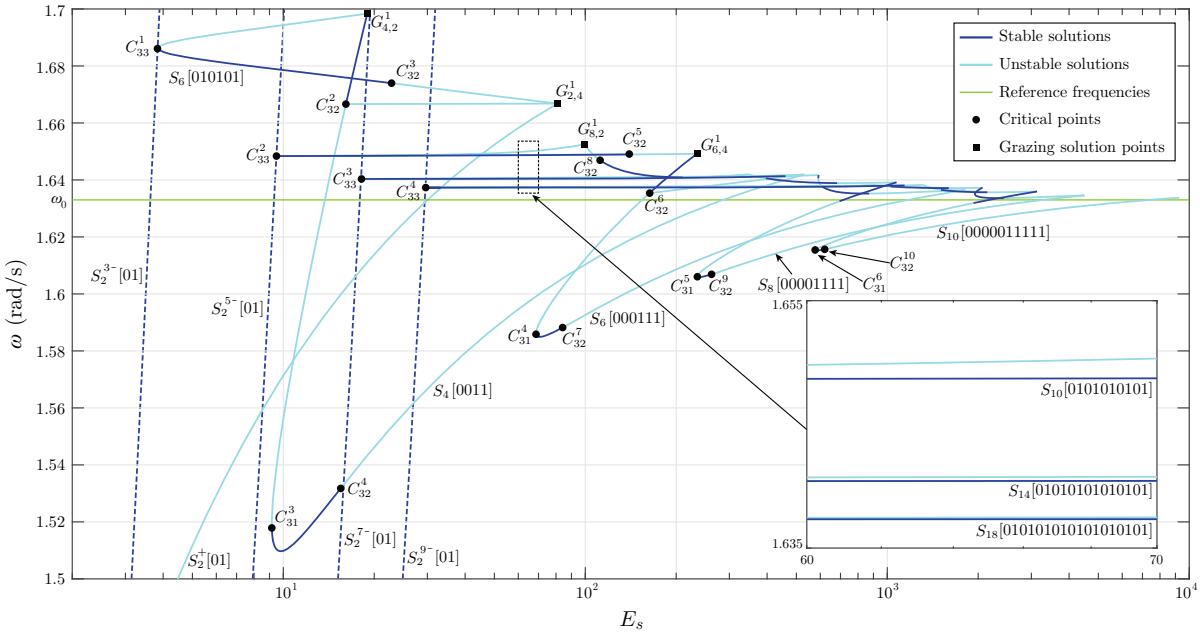

Fig. 10 FEP of the path consisted of symmetric branches succeeding S_0^+

To provide more insight of the FEP's structure, the time histories and phase portraits at selected points on these major branches are shown below. First, responses at critical points C_{32}^3, C_{32}^5, C_{32}^{11} and C_{32}^{12} on branches corresponding to, respectively, $k = 3, 5, 7$ and 9 in the $S_{2k}[01]^k$ family are plotted in Fig. 12. Such solutions have impacts happening successively on the two sides so that the time histories appear in a 'chattering' manner, and such branches seem to appear only above the frequency level ω_0 while approaching ω_0 with increasing number of impacts involved in a period. Meanwhile, responses at critical points C_{32}^4, C_{32}^7, C_{32}^9 and C_{32}^{10} on branches corresponding to, respectively, $j = 2, 3, 4$ and 5 in the $S_{2j}[0^j 1^j]$ family are plotted in Fig. 13. Such responses share the feature that impacts happen continuously on the same side in half period so that the time histories appear in a sticking manner, and the lowest frequency on such branches is always below ω_0 and approaches ω_0 with increasing number of impacts. In some sense, the main body of the symmetric path of FEP is clamped between the frequency-maximizing points on $S_{2k}[01]^k$ branches and the frequency-minimizing points on $S_{2j}[0^j 1^j]$ branches. As energy approaches infinity while frequency is limited around ω_0, the clearance will be ignorable compared to the amplitude of vibration, and both $S_{2k}[01]^k$ and $S_{2j}[0^j 1^j]$ solutions approach the response form where the masses vibrate synchronously as if one is fixed on another so that the system collapses to a single-DOF linear system whose natural frequency is exactly ω_0, corresponding to a predicted convergence to ω_0 at infinite energy on the FEP.

Among all observed critical points, those in the C_{33} family deserve particular attention. In the FEPs shown above, such points appear only as the bifurcation points where a duplicate branch $S_2^{k-}[01]$ meets its counterpart in the $S_{2k}[01]^k$ family, as is the case for C_{33}^1, C_{33}^2, C_{33}^3 and C_{33}^4. Notice that k must be an odd number for a duplicate branch $S_2^{k-}[01]$ to bifurcate into a symmetric branch, since the condition for symmetry $z(t + T/2) = -z(t)$ can never be met by an $A_{2k}[01]^k$ branch when k is even. However, it is worth noting that similar critical points can also emerge on duplicate branches $S_2^{k-}[01]$ when k is even. An example is given as the bifurcation on duplicate branch $S_2^{4-}[01]$, as shown in Fig. 14, where a piece of the symmetric path is taken by omitting the branches beyond the grazing solution point $G_{4,4}^1$. Emphasis is laid on the critical point C_{32}^4 on branch $S_4[0011]$, where it bifurcates into another asymmetric branch $A_4[0011]$ that was previously omitted in discussions about the symmetric path. The $A_4[0011]$ branch is then connected

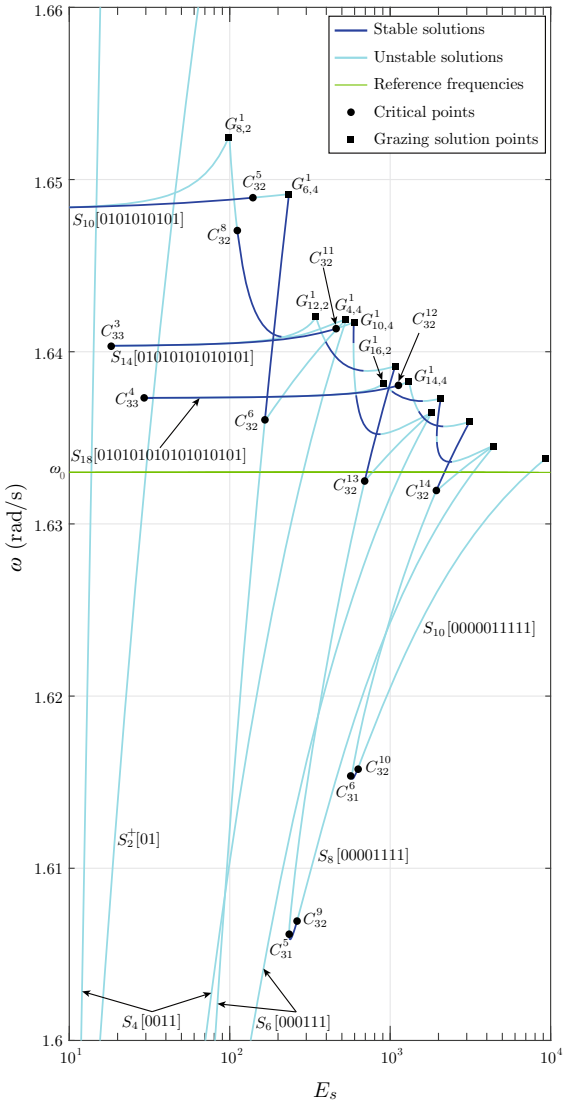

Fig. 11 FEP of the path consisted of symmetric branches succeeding S_0^+: details at high energy levels, labels omitted for trivial branches and critical/grazing solution points

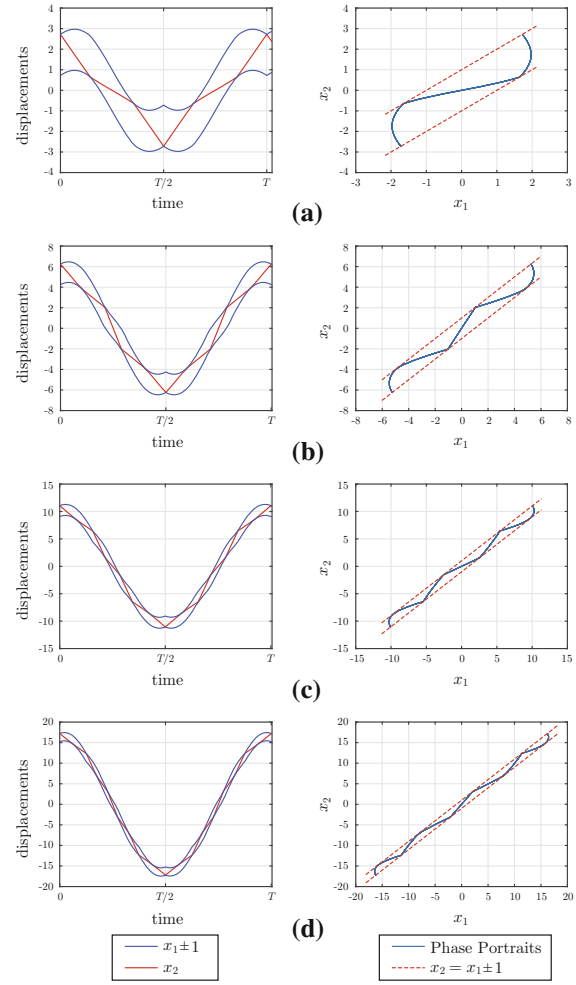

Fig. 12 Time histories and phase portraits at selected solution points on branches in the $S_{2k}[01]^k$ family: **a** C_{32}^3; **b** C_{32}^5; **c** C_{32}^{11}; **d** C_{32}^{12}

through an $A_6[001011]$ branch to an $A_8[01010101]$ branch, which meets the duplicate branch $S_2^{4-}[01]$ at the critical point C_{33}^5. When the $A_8[01010101]$ branch bounces back from C_{33}^5, it leads to a tongue consisted of branches that increase successively in the number of impacts but are localized both in frequency and energy on the FEP. Details of this region as framed by dashed lines in Fig. 14 are depicted in Fig. 15. Every branch in such tongue shares the features that it has two short stable segments at low frequency levels, it bifurcates once at a C_{22} critical point and all of its ends meet its neighbors' at certain grazing solution points. The time histories and phase portraits at critical points C_{22}^1, C_{22}^2, C_{22}^3, C_{22}^4 are shown in Fig. 16, indicating that such a local tongue of asymmetric branches represents a family of responses that are sticking at one side while maintaining only 2 impacts at the other side. Regarding such tongue as an extension from the symmetric branch $S_4[0011]$, it is predicted that similar tongues will extend from all branches in the previously defined $S_{2j}[0^j 1^j]$ family, and they each should involve the bifurcation from a corresponding duplicate branch $S_2^{k-}[01]$ with $k = 2j$ which is even.

It has been revealed above that branches bifurcating from the duplicate branches $S_2^{k-}[01]$, $k \geq 3$ are

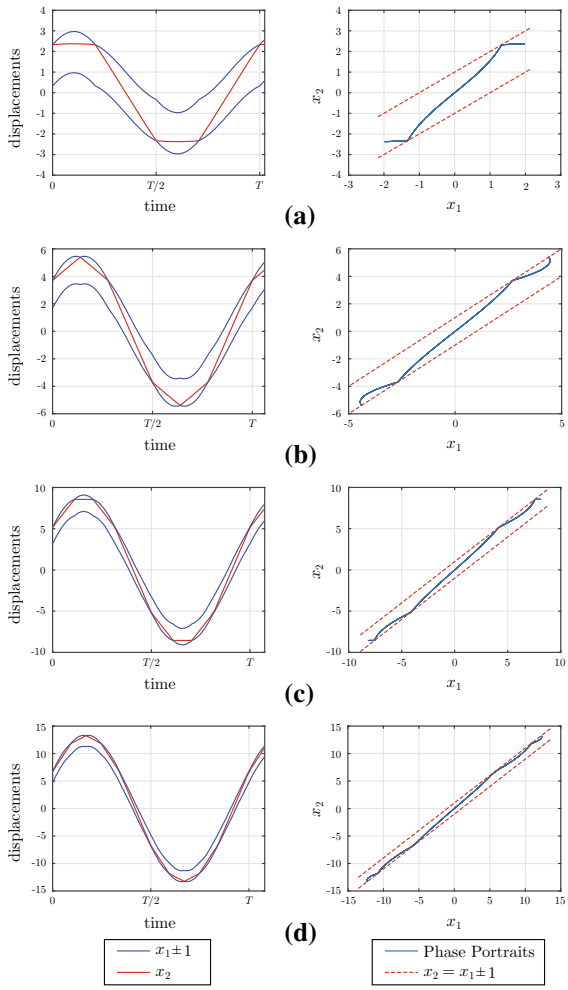

Fig. 13 Time histories and phase portraits at selected solution points on branches in the $S_{2j}[0^j 1^j]$ family: **a** C_{32}^4; **b** C_{32}^7; **c** C_{32}^9; **d** C_{32}^{10}

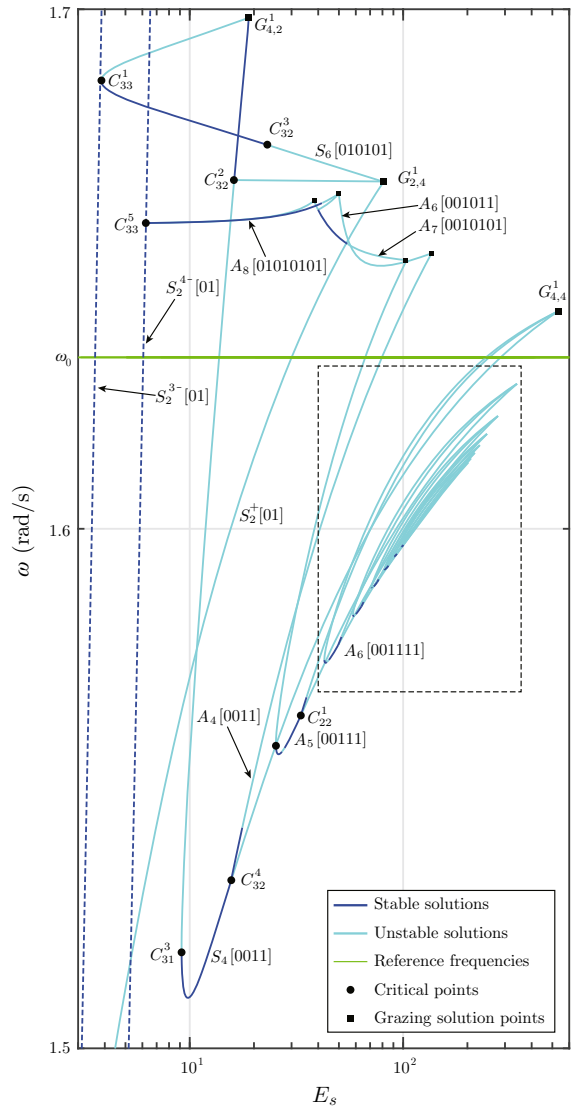

Fig. 14 FEP including bifurcations from the duplicate branch $S_2^{4-}[01]$

connected together to form the major body of FEP within frequency range $[\omega_1\ \omega_2]$, including both the symmetric path and the asymmetric single-side sticking tongues. Besides, a special case is discovered when dealing with the bifurcation happening on duplicate branch $S_2^{2-}[01]$, as shown in Fig. 17. Unlike the cases of other $S_2^{k-}[01]$ branches when k is even, there are no tongues of single-side sticking branches. Instead, a closed loop composed of asymmetric branches exclusively appears, with selected time histories and phase portraits shown in Fig. 18. It is thus concluded that all duplicate branches $S_2^{k-}[01]$, $k \geq 2$ each meet a C_{33} critical point within frequency range $[\omega_0\ \omega_2]$ and bifurcate into branches that further construct the main body of FEP within frequency range $[\omega_1\ \omega_2]$. In the following, this part of the FEP along with branch $S_2^-[01]$ is dubbed the elementary structure, which is composed of all components shown in Figs. 3, 8, 10, 14 and 17 plus all further branches extending from them (including those on the symmetric path, on local single-side sticking tongues, on the closed loop bifurcating from $S_2^{2-}[01]$, and trivial asymmetric side branches). The above presents all observations on the FEP within frequency range $\omega \geq \omega_1$, and the section is concluded by a partial view of the entire elementary structure as shown in Fig. 19.

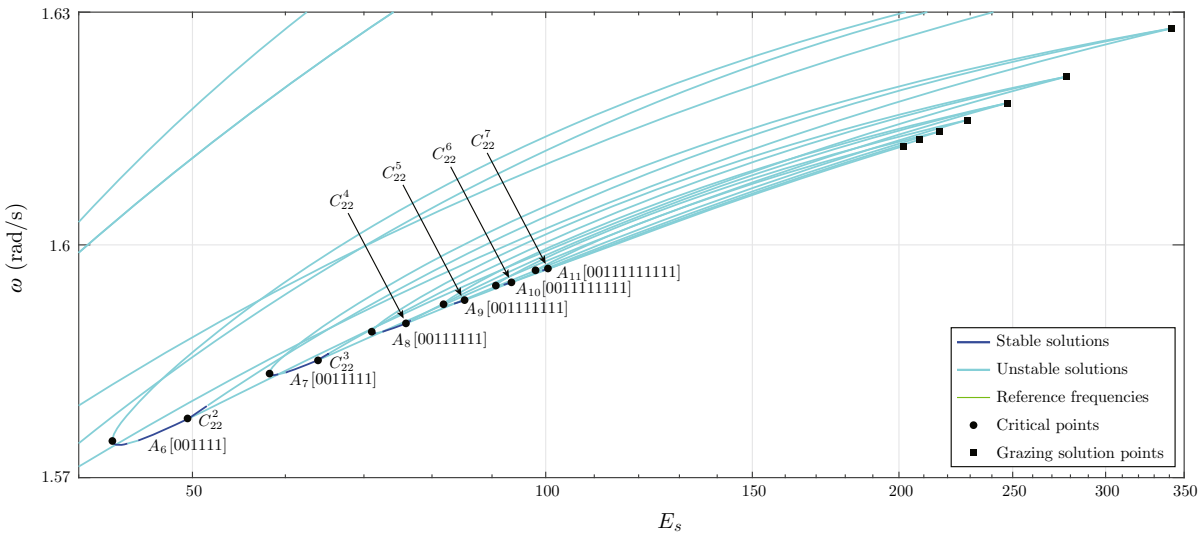

Fig. 15 Zoomed-in view of the local tongue composed of single-side sticking responses

3.2 Complete FEP as infinite fractals

3.2.1 Bifurcations at grazing solution points and extra critical points on duplicated branches

The elementary structure depicted till this point, however, is not the whole picture. The C_{33} critical points discovered so far are not the only ones on the duplicate branches $S_2^{k-}[01]$, and in fact, it is observed that a duplicate branch $S_2^{k-}[01]$ typically has $k-1$ critical points in the C_{33} family, as shown in Fig. 20a, where the duplicate branches corresponding to k from 2 to 9 along with the original $S_2^{-}[01]$ branch are shown. As marked in red arrows, some of the extra C_{33} points are duplicates, i.e., a duplicate branch $S_2^{k-}[01]$ will always contain the duplicate C_{33} points whose origins lie on duplicate branches $S_2^{j-}[01]$, where j is an integer divisor of k. There are, however, still extra C_{33} points that are original, such as C_{33}^7, C_{33}^8, C_{33}^9 and C_{33}^{10} in Fig. 20a. These points are about to give birth to new branches that are in general more complicated in nature and are not duplicates of any branch already found. Furthermore, so far only duplicates of the $S_2^{-}[01]$ branch are studied, and there is nothing preventing similar extra critical points to appear on duplicates of all the other original branches. For example, the duplicates of the original $S_2^{+}[01]$ branch are investigated and shown in Fig. 20b, where the frequency axis is also given in log scale. It seems to share the same feature that a duplicate branch $S_2^{k+}[01]$ has $k-1$ critical points in the C_{33} family. However, such feature is no longer true when the duplicates of the original $A_1[0]$ branch (as in Fig. 17) are investigated, as shown in Fig. 20c. It appears that the first extra C_{33} point, labeled as C_{33}^{11}, did not appear on the admissible branches until $k=4$. However, it turns out that C_{33} points may have already shown up on the inadmissible part of the branches, as plotted in red lines in Fig. 20c, but are omitted until they fall on the admissible part. Such fact makes it nearly impossible to predict the number of extra C_{33} points on each duplicate branch, and it is thus assumed that the number of extra critical points on duplicate branches is highly dependent on the form of the original branch.

At the same time, it deserves particular attention that the loop shown in Fig. 17 ends at the grazing solution point $G_{0,4}^1$, which is also the end of the duplicate branch $S_2^{2-}[01]$. Such fact passes the message that a duplicate grazing solution point on duplicate branches may trigger new branches that cannot be found on the original one. Specifically, suppose that an original branch ends at a grazing solution point in the $G_{N,p}$ family, which is the potential end of up to 2^p separate branches, and as a result a k-duplicate of the branch will end at a duplicate of the grazing solution point, which will naturally be in the $G_{kN,kp}$ family and thus can be the potential end of up to 2^{kp} branches. Therefore, due to the existence of extra critical points and duplicate grazing solution points, it is then expected that there exist extremely

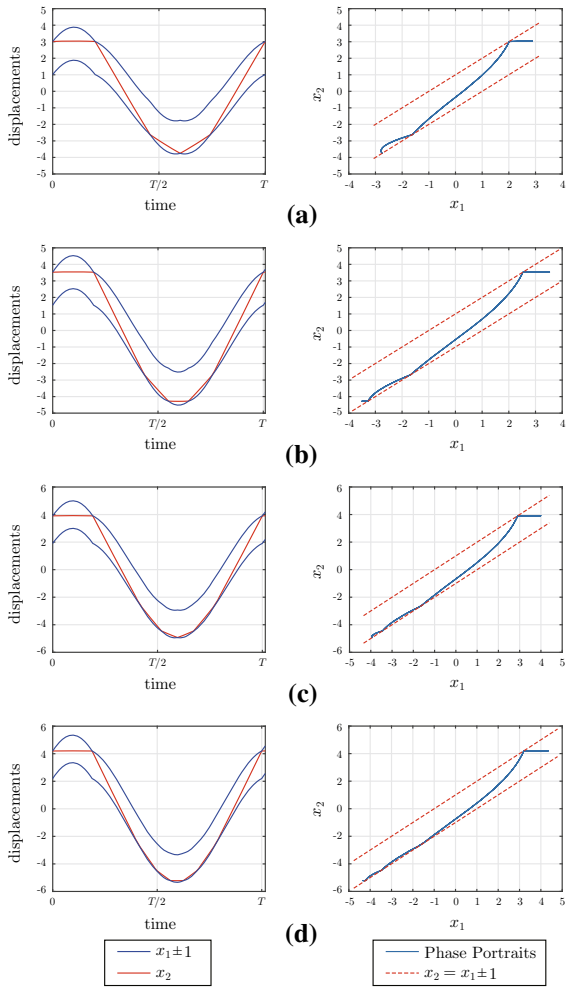

Fig. 16 Time histories and phase portraits at selected solution points on branches depicted in Figs. 14 and 15: **a** C_{22}^1; **b** C_{22}^2; **c** C_{22}^3; **d** C_{22}^4

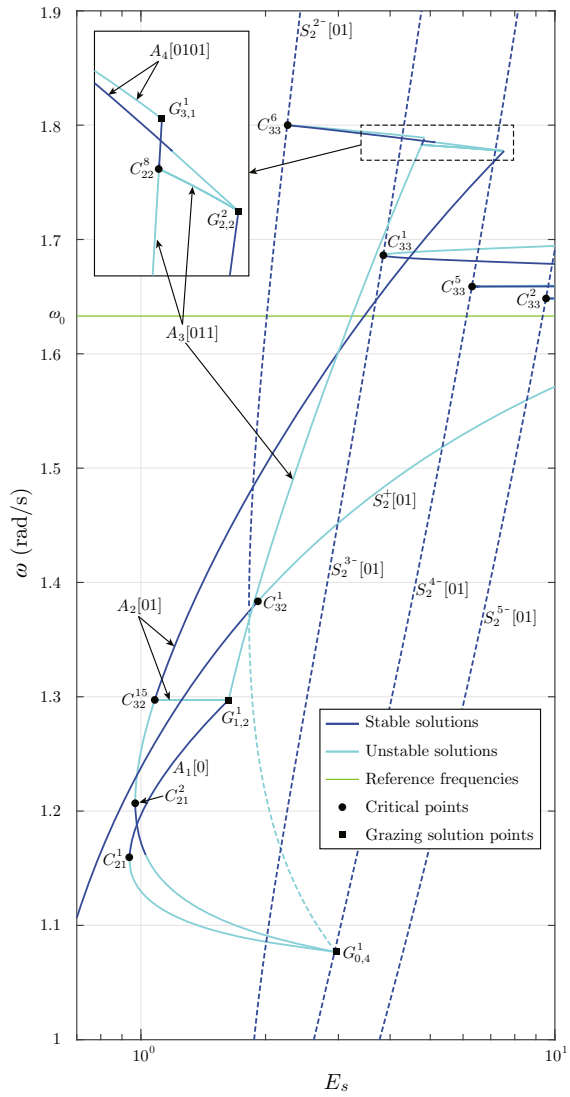

Fig. 17 FEP of a closed loop consisted of asymmetric branches bifurcating from C_{33}^6 and ending at $G_{0,4}^1$ on the same duplicate branch $S_2^{2-}[01]$

complicated hidden topologies in the lower-frequency domain on the FEP, including the extra branches starting from the duplicates of the grazing solution points that have been found as well as those starting from extra C_{33} critical points that theoretically may emerge on the duplicates of any branch. Moreover, it is observed that the C_{33} critical points only appear on the stable parts of a duplicate branch.

3.2.2 Fractal bases on FEP

The entire FEP can be then visualized as follows. Consider any original branch $A_N[R]$ that has been found, C_{33} points may emerge on any of its k-duplicates, and each C_{33} point leads to a bifurcation. Then, any new original branch $A_{kN}[R]^k$ bifurcated from a C_{33} point on a k-duplicate of $A_N[R]$ can find its own j-duplicate bifurcating from the (kj)-duplicate of $A_N[R]$. Any j-duplicate of $A_{kN}[R]^k$ can now give birth to new original branches $A_{jkN}[R]^{kj}$, and so on. Therefore, it is claimed that the FEP should be generated following a pattern of infinite fractals toward zero frequency. In order to illustrate this, several notations need to be introduced. First, a general notation is used for both original and duplicate branches as $A_N^k[R]\{F_p^j\}$, where

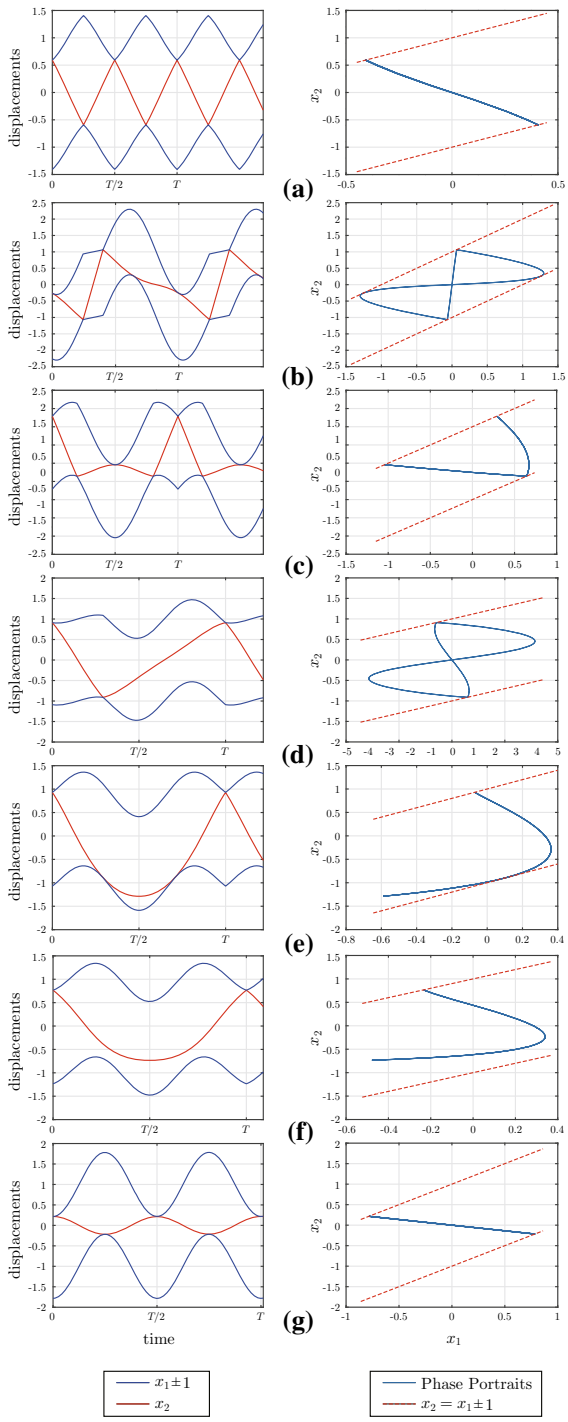

Fig. 18 Time histories and phase portraits at selected solution points on branches depicted in Fig. 17: **a** C_{33}^{6}; **b** $G_{2,2}^{2}$; **c** $G_{3,1}^{1}$; **d** C_{32}^{15}; **e** $G_{1,2}^{1}$; **f** C_{21}^{1}; **g** $G_{0,4}^{1}$

N and R define the number and sides of the impacts in the response form of its corresponding original branch, respectively, and k states that the current branch is the k-duplicate of its origin so that $k = 1$ for any original branch. Define fractal bases F_p^j, $p = 1, 2$, as sets of branches. An F_1^j base consists of $S_2^{j+}[01]$, which is the j-duplicate of the $S_2^{+}[01]$ branch, and all branches that can be connected to it through a path that successively connects any number of branches, no matter original or duplicate, but does not include any duplicate or original $S_2^{-}[01]$ or $S_2^{+}[01]$ branches. An F_2^j base consists of $S_2^{j-}[01]$ and all branches that can be connected to it in a similar way, but are not included in any F_1^i base. As an example, the elementary structure shown previously should be the combination of fractal bases F_1^1, F_2^1 and F_2^2. And finally, the notation $A_N^k[R]\{F_p^j\}$ for a branch states that its origin lies in the F_p^j base, and typically an $A_N^k[R]\{F_p^j\}$ branch itself should lie in base F_p^{jk}. The complications in the notations can be viewed as a consequence of the interactions between the two basic backbone branches $S_2^{\pm}[01]$, which are further due to the dislocations in frequency between their duplicates.

For example, the fractal base F_2^6 is depicted in Fig. 21. The backbone is notated as $S_2^{6-}[01]\{F_2^1\}$, which is simply $S_2^{6-}[01]$ in previous notations. As mentioned before, it has in total 5 C_{33} critical points, among which C_{33}^{61} and C_{33}^{65} lead to original branches that should be denoted as $A_{12}^{1}[010101010101]\{F_2^6\}$. Meanwhile, referring to Fig. 20, C_{33}^{62} is the 2-duplicate of C_{33}^{1}, C_{33}^{63} is the 3-duplicate of C_{33}^{6} and C_{33}^{64} is the 2-duplicate of C_{33}^{7}. Notice that by definition, branches bifurcating from C_{33}^{62} and C_{33}^{61} in fact belong to fractal bases F_1^2 and F_1^1, respectively, but are plotted here for clarification. Referring to Fig. 19, C_{33}^{61} leads to the second single-side sticking tongue in the elementary structure. Meanwhile, branches bifurcating from C_{33}^{62} are 2-duplicates of the first 'chattering' branches in the symmetric path and C_{33}^{63} leads to 3-duplicates of branches in the closed loop in the elementary structure. Moreover, C_{33}^{64} leads to the 2-duplicate of a closed loop in base F_2^3, and C_{33}^{65} leads to an original loop. All these loops end at duplicates of the grazing solution point $G_{0,4}^{1}$, and it is predicted that there would be an infinite number of loops appearing in the infinite fractal base F_2^{∞}. In fact, an F_2^j base shall only include the bifurcated branches that form loops since others typically will connect to F_1^i bases, like the bifurcations at C_{33}^{62} and C_{33}^{61}. Yet a more

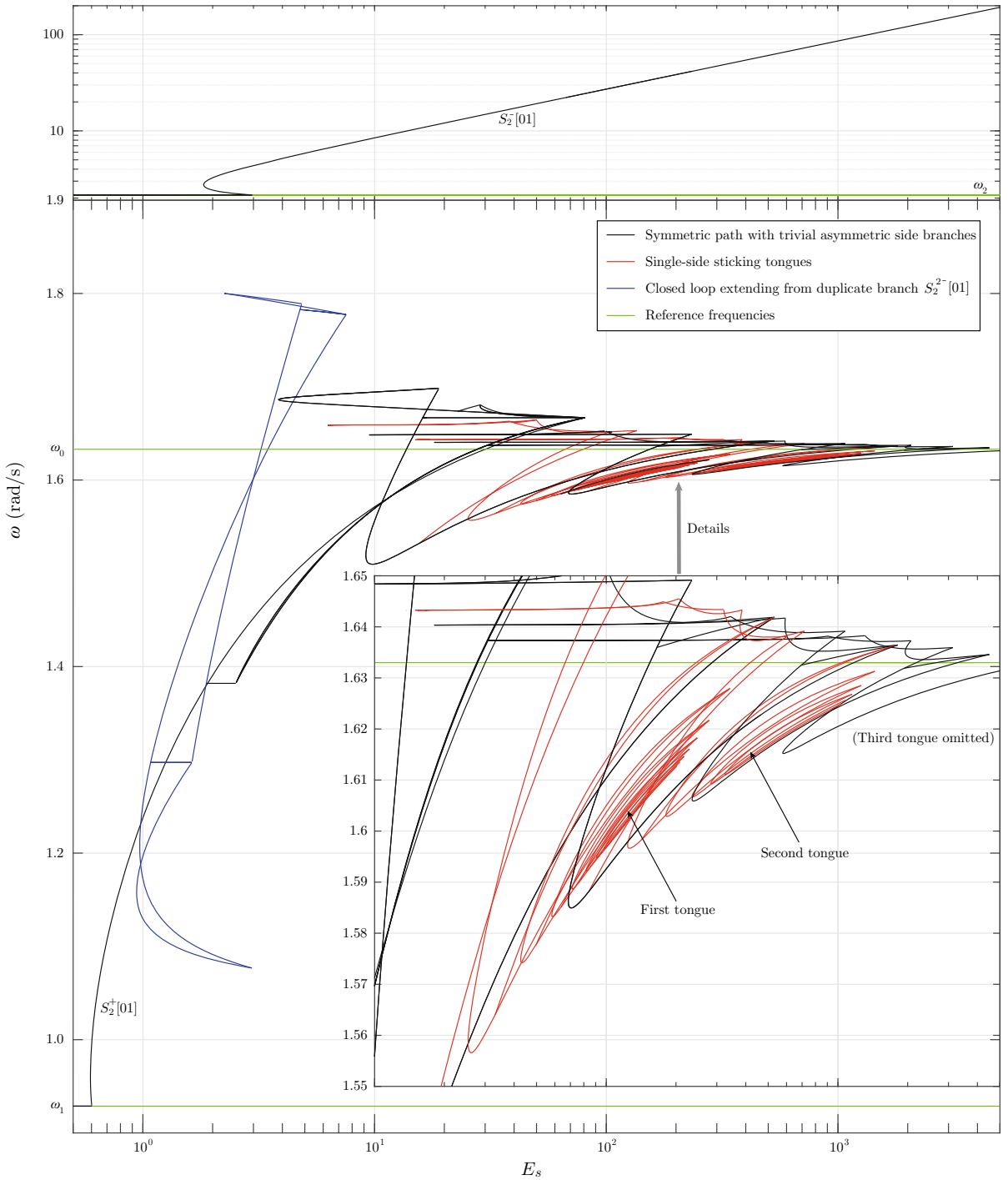

Fig. 19 General view of the elementary structure of FEP within frequency range $\omega \geq \omega_1$: two single-side sticking tongues shown in red; trivial side branches at low energy levels shown in black but omitted at high energy levels; region above 1.9 rad/s shown in log scale to fully depict the $S_2^-[01]$ branch. (Color figure online)

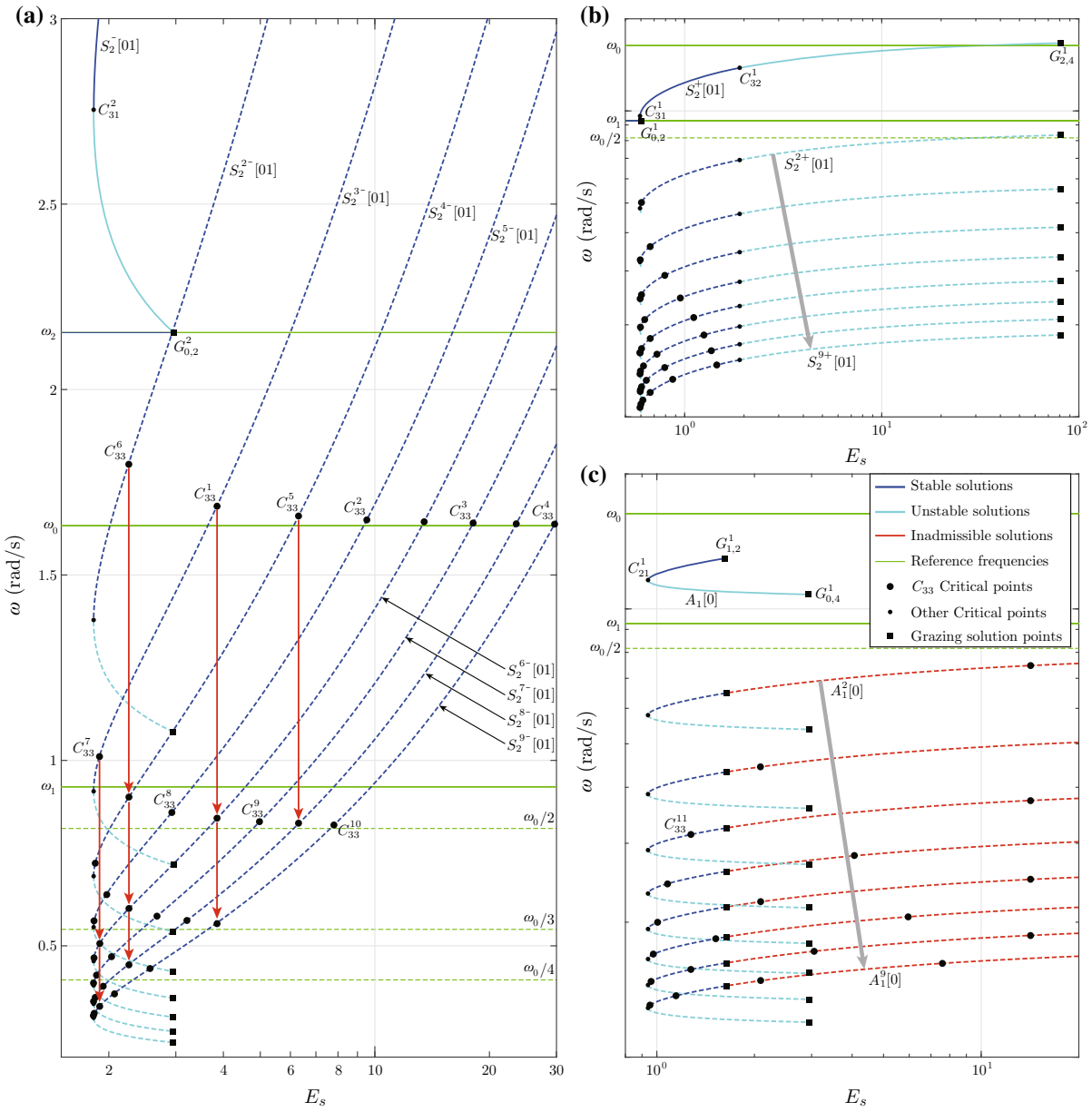

Fig. 20 FEPs including duplicates of selected original branches, with example C_{33} critical point inheritances shown in red arrows: **a** duplicates of $S_2^-[01]$; **b** duplicates of $S_2^+[01]$; **c** duplicates of $A_1[0]$. (Color figure online)

exciting observation is made on the duplicate branches bifurcating from C_{33}^{62} and C_{33}^{63}, shown in Fig. 21d and **e**. As expected, sub-level critical points C_{33}^{66} and C_{33}^{67} emerged and led to original local closed loops whose topologies are similar to the larger-scale loops shown in Fig. 21b. The potential fractal structure can be partially illustrated by the observations above if one assumes bifurcations will continue to occur on further duplicates of the original branches in the loops shown in Fig. 21d, e, and so on.

Conventionally, the bifurcations at such C_{33} points are understood as internal resonances [33], due to observations on the elementary structure that these points correspond to locations where the frequency of

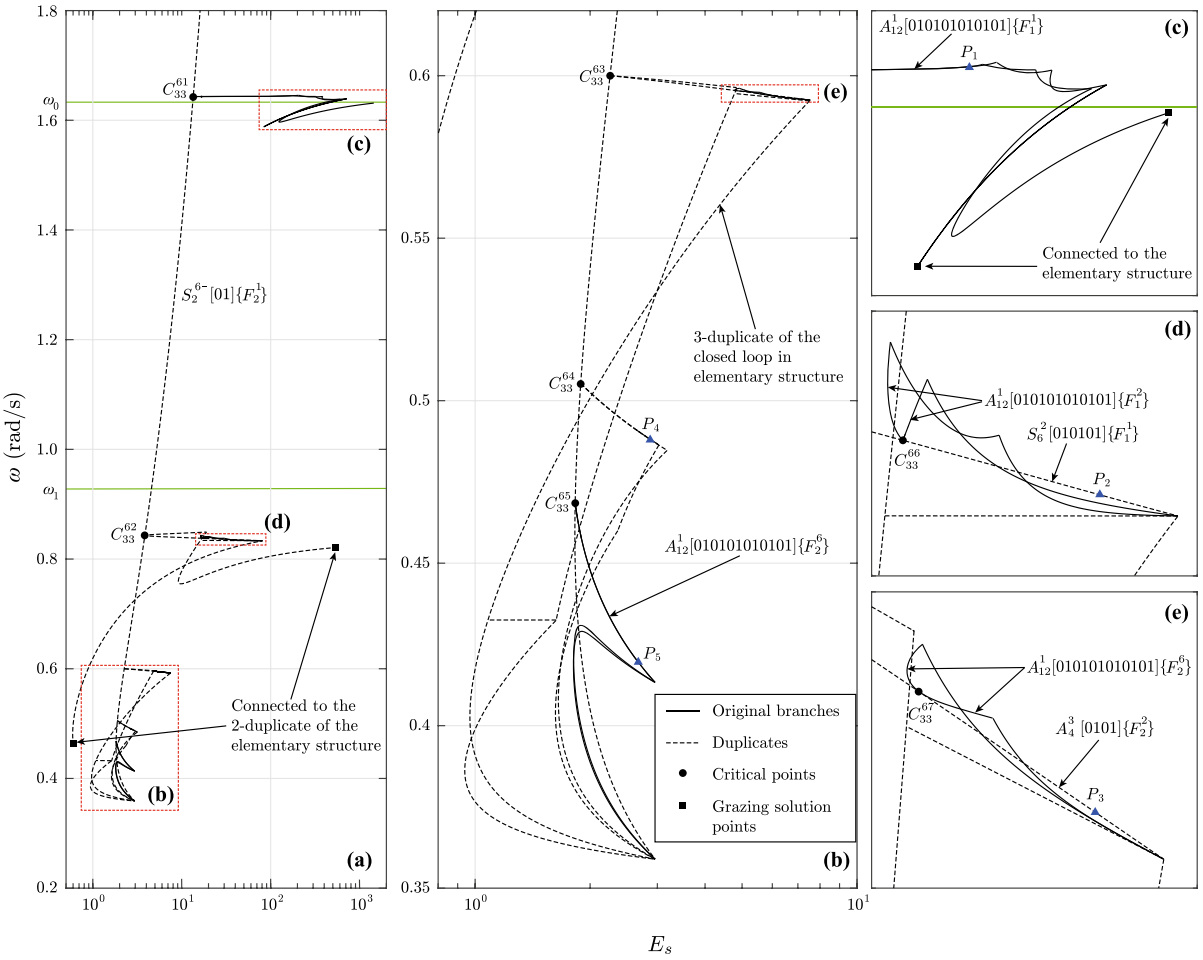

Fig. 21 FEP including branches in fractal base F_2^6 along with related branches in F_1^i bases: **a** overview; **b** closed loops in F_2^6; **c** bifurcations out of C_{33}^{61}; **d** and **e**: original sub-level closed loops

branches on the symmetric path is an odd-number divisor of the $S_2^-[01]$ backbone, as is the case for points C_{33}^1, C_{33}^2, C_{33}^3 and C_{33}^4. However, this may not be general enough since it is found that these bifurcations can also lead to closed loops that don't correspond to obvious interactions between the two families of fractal bases F_1^i and F_2^j. Therefore, the following discussions will be focused on their period-multiplying nature, i.e., a C_{33} bifurcation where the k-duplicate $A_N^k[R]\{F_p^i\}$ of any original branch $A_N^1[R]\{F_p^i\}$ bifurcates into original branches $A_{kN}^1[R]^k\{F_{p'}^j\}$ is an instance of k-time period multiplying so that, for example, $k = 2$ gives period doubling and $k = 3$ gives period tripling. Furthermore, since a C_{33} point itself can be a duplicate, as is the case for C_{33}^{62}, C_{33}^{63} and C_{33}^{64} in Fig. 21, in general a C_{33} bifurcation on a k-duplicate branch could represent a j-time period multiplying where j is an integer divisor of k. For demonstration, the time histories and phase portraits corresponding to 5 selected regular solution points P_1 to P_5 on the FEPs in Fig. 21 are depicted in Fig. 22, where they each represent a C_{33} bifurcation. Meanwhile, the idea can be explained best by plotting all the responses at the corresponding C_{33}^{6i} points, $i = 1, 2, 3, 4, 5$, but by assuming that response shapes along the backbone branch $S_2^{6-}[01]\{F_2^1\}$ are similar in appearance, only that at C_{33}^{63} is picked as example. Notice that though the periods (original or multiplied) at these points are essentially different, they are scaled to have the same number of impacts on the plots in order to show intuitive comparisons among the response shapes. Briefly, P_1 and P_5 are original in

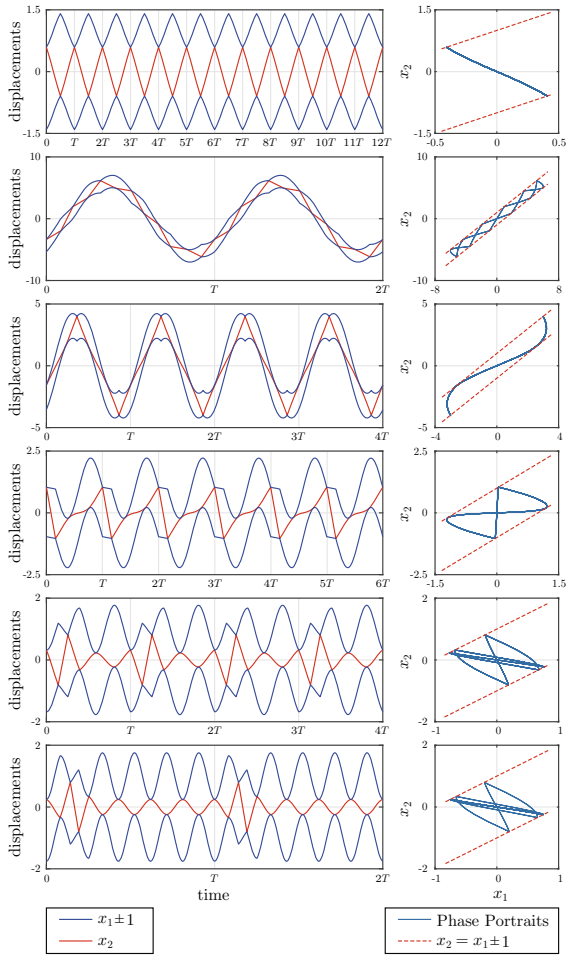

Fig. 22 Time histories and phase portraits at selected points in Fig. 21. From top to bottom: C_{33}^{63}; P_1; P_2; P_3; P_4; P_5

base F_2^6 so that they both correspond to period sextupling, while P_2 and P_4 are 2-duplicates of their original points, respectively, so that they correspond to period tripling and finally P_3 is the 3-duplicate of its origin so that it stands for period doubling. By this point, it needs to be clarified that only the bifurcations where duplicate branches transit into original branches are instances of period multiplying, which typically occur at C_{33} critical points, while period is continuously maintained during bifurcations at other critical or grazing solution points that only involve original branches.

An interesting aspect of interpreting the C_{33} bifurcations as period multiplying lies in its further potential to form cascades. Consider an original branch which is the result of a first-level period multiplying, and then C_{33} bifurcations on its own duplicates will represent a second-level period multiplying, and so on. To clearly present the concept, a slice of the deep fractal base F_1^8 is investigated, as shown in Fig. 23. Briefly, the lower part of the 8-duplicate of the first 'chattering' branch $S_6[010101]$ in the elementary structure, referring to Fig. 10, is investigated, corresponding to a C_{33} bifurcation from the 24-duplicate of the backbone $S_2^-[01]$. This branch, $S_6^8[010101]\{F_1^1\}$, appears to also hold the feature that it has 8-1=7 extra C_{33} points, labeled as C_{33}^{8i}, i from 1 to 7. Since the divisors of 8 are 2 and 4, it only inherits 3 critical points from the 4-duplicate which are C_{33}^{82}, C_{33}^{84} and C_{33}^{86}, where C_{33}^{84} is further inherited from the 2-duplicate and its origin is exactly C_{33}^{66} in Fig. 21d, and thus, all the other 4 points C_{33}^{81}, C_{33}^{83}, C_{33}^{85} and C_{33}^{87} lead to original branches that are in the form $A_{48}^1[01]^{24}\{F_1^8\}$, which corresponds to period octupling. Focusing on point C_{33}^{84} (the 4-duplicate of C_{33}^{66}), a new critical point C_{33}^{88} emerges on the duplicate branch $A_{12}^4[01]^6\{F_1^2\}$ and leads to original branches in the form of $A_{48}^1[01]^{24}\{F_1^8\}$. Then, an example cascade of period multiplying can be tracked along the path marked in red in Fig. 23a. According to previous discussions, the bifurcations at C_{33}^{80} (which is the 8-duplicate of C_{33}^1), C_{33}^{84} and C_{33}^{88} will involve transitions in the form of period tripling, period doubling and period quadrupling, respectively. Similar to Fig. 22, the time histories and phase portraits at the 3 critical points as well as at $G_{46,2}^1$, the end of the path, are given, where the time axes are scaled so that the depicted responses each include 48 impacts. Moreover, the cascade is exhibited as bifurcation diagram in Fig. 23c, where the displacement x_2 at all impacting instants within one period are plotted against the accumulated distance travelled on frequency axis along the path marked in red.

3.2.3 Summary of observations

In conclusion, the entire FEP of the impacting system should include all fractal bases F_p^k, $p = 1, 2$, $k = 1, 2, 3, \ldots$, and each base F_p^k should include duplicates of all branches in all bases F_p^j, where j is an integer divisor of k. Meanwhile, new C_{33} critical points (that have no counterparts in any parent base F_p^j) will emerge on these duplicate branches in F_p^k, so that bifurcations corresponding to period multiplying will lead to new original branches in F_p^k which will further transit (at grazing solution points) into original branches until connecting with an existing branch, which may involve

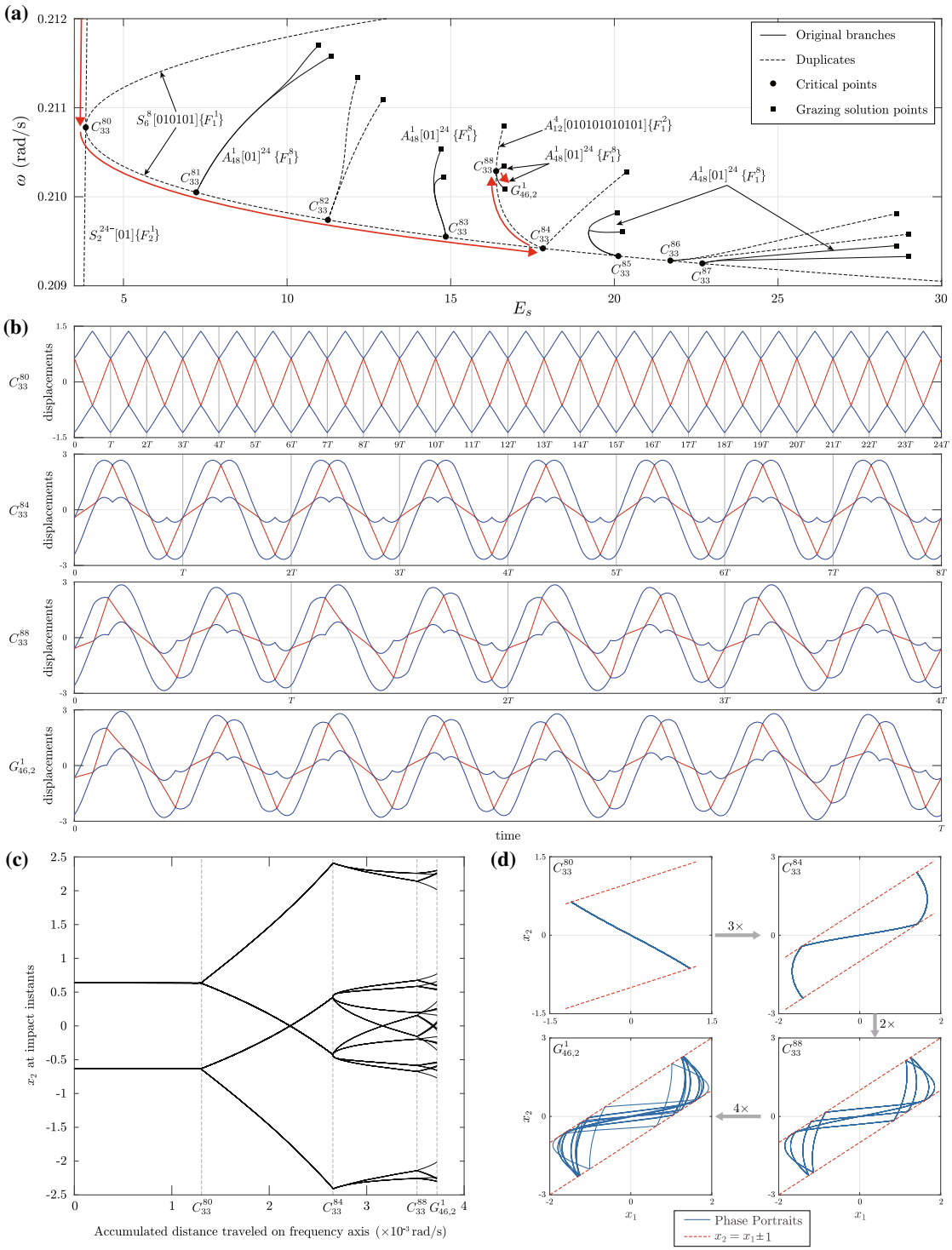

Fig. 23 An example of period-multiplying cascade in fractal base F_1^8: **a** FEP; **b** time histories at representative points; **c** bifurcation diagram generated by recording x_2 at impacting instants for each solution point on the path shown in **a**; **d** corresponding phase portraits. (Color figure online)

interactions among different bases. In other words, the structure of F_p^k should be richer than the union of all duplicated F_p^j's. Till this point, assumptions may be made regarding features of the two infinite bases F_p^∞, $p = 1, 2$, which should be infinitely close to zero frequency on the FEP. First, any stable branch corresponding to periodic orbits in F_p^∞ would be a duplicate that have an infinite number of C_{33} critical points on it. Thus, an infinite number of paths can be found that represent cascades of period multiplying, similar to the one in Fig. 23a. The end of any of these pathes will correspond to pseudo-periodic responses that have an infinite period so that they can be considered as the only original branches in F_p^∞ and are likely in the form of chaos. In other words, any periodic response, no matter how large the period is, should lie in either infinite base F_p^∞ as a duplicate solution point and any pseudo-periodic response that is the product of cascades of period multiplying should be found as an original solution point. Yet conversely, it is still unclear whether all pseudo-periodic or chaotic response triggered by arbitrary initial conditions are in essence the outcome of such bifurcations.

3.3 Analogy to systems with polynomial nonlinearities

As mentioned before, a potential significance of the present work lies in that the impacting system is essentially related to a family of systems with polynomial nonlinearities. Recall the general EOMs for such systems

$$\begin{cases} m_1\ddot{u}_1 + (k_1+k_2)u_1 - k_2u_2 = \dfrac{k_2(u_2-u_1)^n}{d^{n-1}} \\ m_2\ddot{u}_2 - k_2u_1 + k_2u_2 = -\dfrac{k_2(u_2-u_1)^n}{d^{n-1}} \end{cases}, \tag{50}$$

which can be scaled, by $x_i = u_i/d$, into

$$\begin{cases} m_1\ddot{x}_1 + (k_1+k_2)x_1 - k_2x_2 = k_2(x_2-x_1)^n \\ m_2\ddot{x}_2 - k_2x_1 + k_2x_2 = -k_2(x_2-x_1)^n \end{cases}, \tag{51}$$

where n is odd, and previous discussions on the impacting system should correspond to $n \to \infty$. In this section, the similarities between the FEPs of the impacting system and systems with finite n's will be briefly investigated.

First, the initial part of the symmetric path in the elementary structure is considered, including successive branches S_0^+, $S_2^+[01]$ as in Fig. 3 as well as $S_6[010101]$ and $S_4[0011]$ as in Fig. 10. Their counterparts in the FEPs of system (51) with orders $n = 3$, 7 and 21, under same system parameters (47), are tracked using exactly the same techniques described in [33], as depicted in Fig. 24 in comparison with the impacting system ($n \to \infty$). The shape of the FEPs shows a rather smooth transformation, where it spans more along the energy axis but less on the frequency as n decreases. The stability analysis shows good consistence except around the C_{33}^1 points that the branches with $n = 3$ and 7 are stable after the turning, while branches with $n = 21$ and $n \to \infty$ are stable before it. It is worth noticing that around these bifurcation points, the stable part is always that at lower frequency. Meanwhile, some of the critical points are inherited through the transformation while maintaining the same algebraic and geometric multiplicities for the zero eigenvalue, as is the case for C_{33}^1, C_{32}^1, C_{31}^3 and C_{32}^4. Yet others are shifted due to the deformation of FEP. Moreover, the transformation of the closed loop in the elementary structure along with the 2-duplicate of the backbone $S_2^-[01]$, referring to Fig. 17, is depicted in Fig. 25. It is shown that a system with order n as high as 21 is already able to reveal the twisting corner around $G_{0,2}^2$ in the impacting system's FEP where the linear mode S_0^- transits into $S_2^-[01]$, featuring a short section of unstable solutions and a C_{31} point. Moreover, as there are fewer twists in the shape of FEP as n decreases, some of the bridges cease to exist, leading to generally simpler topologies for lower-order systems.

While the transformations shown above appear to be straightforward, particularly interesting are those happening on the grazing solution points. In general, grazing solution points can only occur when $n \to \infty$, and one may wonder what will be their counterpart when n is finite. In theory, a grazing solution point can hardly be represented by a single critical point since the number of branches bifurcating from a critical point is limited by the geometric multiplicity of the zero eigenvalue, while the number of branches crossing a grazing solution point can be unlimitedly huge depending on the number of grazing instants. Then, it turns out that a grazing solution point in the impacting system's FEP is scattered into a series of critical points in that of systems with finite order n's. In order to show this, the counterpart of the typical grazing solution point $G_{2,4}^1$ investigated previously is sought for $n = 21$, as shown

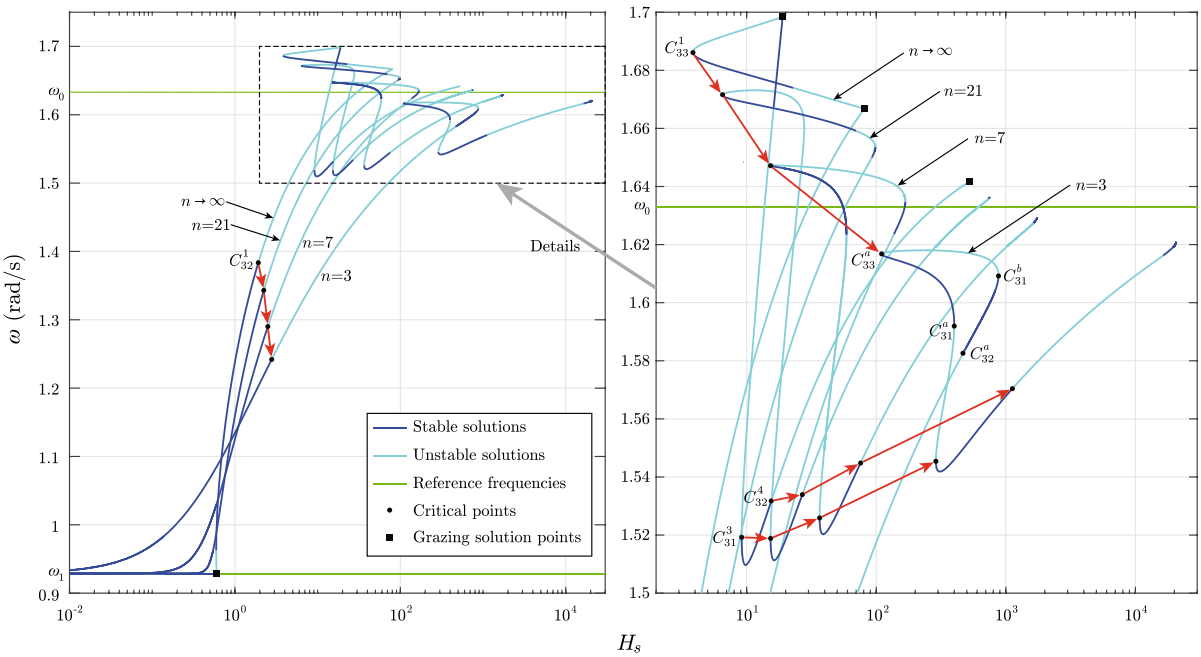

Fig. 24 Deformation of the symmetric path in the elementary structure, at $n = 3, 7, 21, \infty$. (Color figure online)

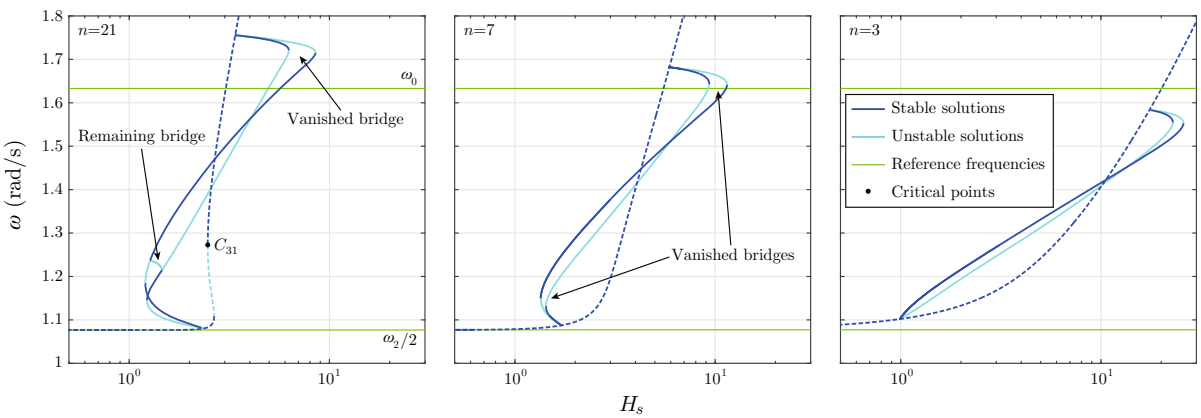

Fig. 25 Deformation of the closed loop in FEPs of systems with finite order n's, in comparison with $n \to \infty$ in Fig. 17

in Fig. 26. Referring to Figs. 7 and 8, there is expected to be 5 more branches crossing $G^1_{2,4}$ that accompany the symmetric path as trivial side branches. However, it seems that only 3 of them have counterparts at $n = 21$. First, the end of the horizontal $S_4[0011]$ bridge is now at C^b_{32}, which was supposed to be the other ends of two vanished trivial branches $A_4[0101]$ and $A_5[00101]$ in Fig. 7. (To avoid confusions, critical points for systems with polynomial nonlinearities are labeled by superscripts in letters.) Meanwhile, there is expected to exist two branches, as counterparts of $A_4[0010]$ and $A_3[010]$ in Fig. 8, that connect to C^f_{32} on the backbone branch. As shown in Fig. 26, the ends of these two branches are now separated, where one lies at C^d_{32} while the other branch actually bifurcates out of this one at C^e_{32}.

Due to the deformation of FEP and, especially, the scattering of grazing solution points, it is difficult to explicitly describe the map from each solution point of the impacting system onto its counterpart in systems with polynomial nonlinearities. However, intu-

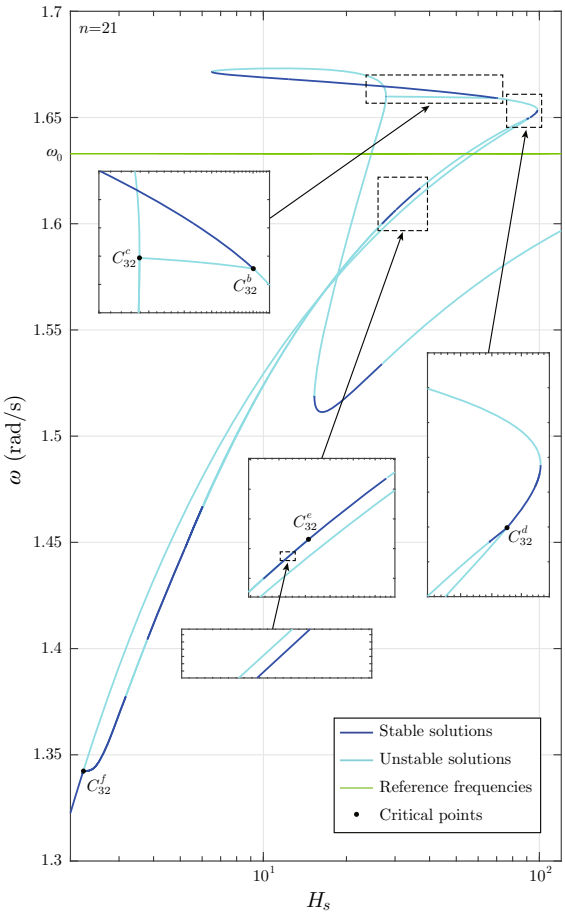

Fig. 26 The scattered grazing solution point $G_{2,4}^1$ at $n = 21$

itive comparisons can be made among responses that show clear correspondences. Referring to Fig. 24, the responses at two critical points C_{33}^1 and C_{31}^3 for the impacting system and their counterparts (marked by red arrows) in systems with $n = 3$, 7 and 21 are compared in Fig. 27. At high orders such as $n = 21$, the responses approximate those of the impacting system so that impact-like reactions are observed when the relative displacement approaches the general clearance $d = \pm 1$. As the order gets lower, such impact-like reactions gradually disappear and $d = \pm 1$ loses its physical meaning, as when $n = 3$. Yet the generally hardening feature of the internal force has ensured similarities in the topologies of the responses. Moreover, the manifolds corresponding to responses refined on the stable segment $\underline{C_{31}^3 C_{32}^4}$ in the impacting system along with their counterparts in the polynomial systems are depicted in Fig. 28, for illustrating the deformation of

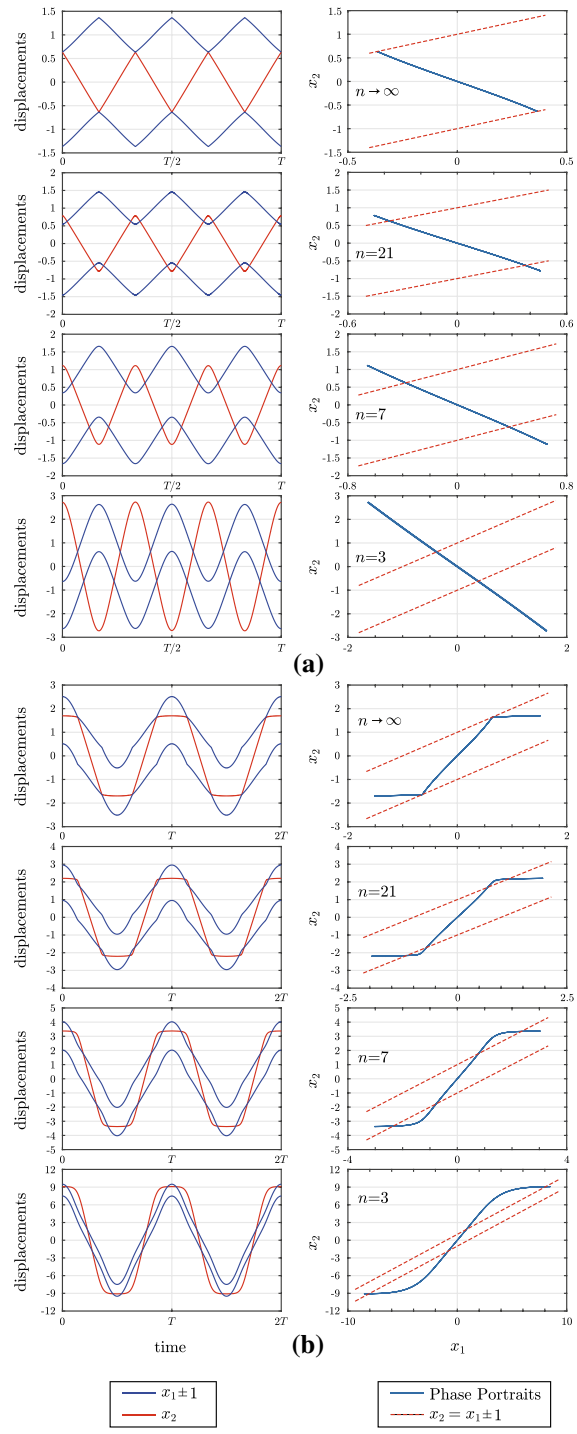

Fig. 27 Time histories and phase portraits at selected solution points in Fig. 24, time axes stretched to fit different period lengths: **a** C_{33}^1 and its counterparts in analogous systems; **b** C_{31}^3 and its counterparts in analogous systems

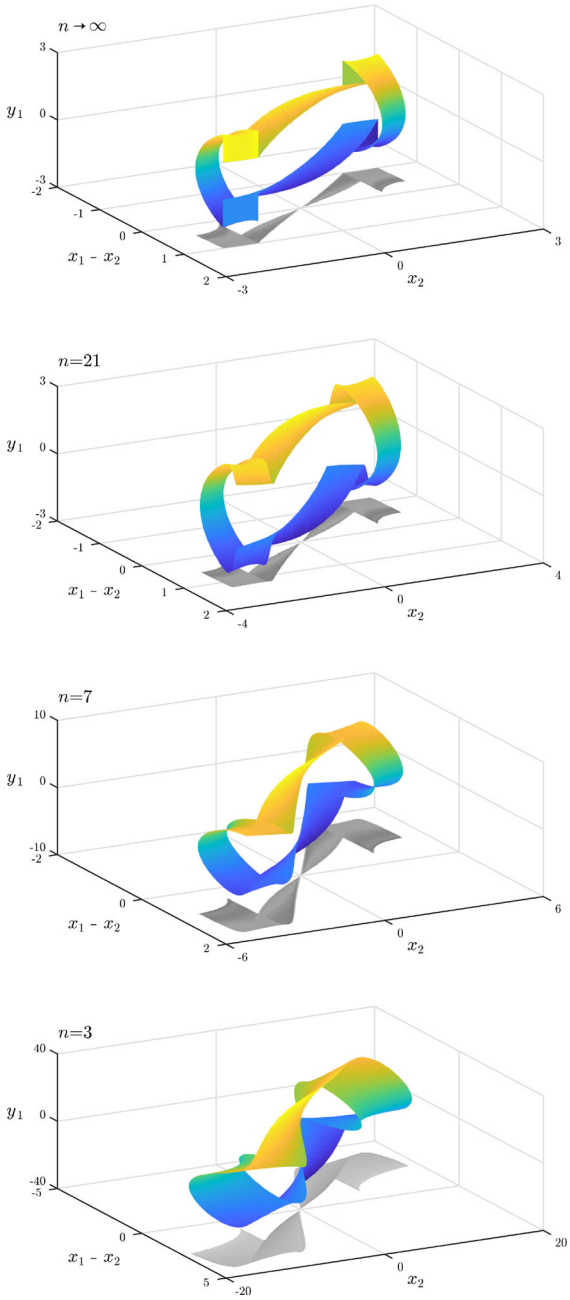

Fig. 28 Manifolds corresponding to the stable segment $\underline{C_{31}^3 C_{32}^4}$ and its counterparts as marked in Fig. 24

orbits. Despite such inherited feature points, the previous notations for branches in the impacting system's FEP may not be general enough to represent FEPs of systems with finite n's. For convenience, in the following, any segment on the FEP will simply be denoted as $A^k|\underline{P_1 P_2}\{F_p^i\}$, where P_1 and P_2 are its end points, k indicates that the segment is the k-duplicate of its origin, and F_p^i is the fractal base where its origin lies. Similar to the case for the impacting system, the fractal bases F_p^i, $p = 1, 2$ are constructed according to connections to the i-duplicates of the in-phase and out-of-phase backbone branches.

Given the evidence for similarities in the NNMs of the impacting system and its analogous systems with finite order n's, it is assumed that the fractal nature is also inherited and one can follow the similar procedures to track C_{33} bifurcations on the duplicate branches at lower-frequency levels for systems with any order n. Consider any original solution point that is already located by continuation, one can simply copy the solutions for initial conditions while multiplying the solution for period by any integer k, and redo the continuation. In this way, a k-duplicate of the original branch can be found, where extra C_{33} bifurcations are expected to happen, leading to new original branches and so on. As counterpart to the bifurcations shown in Fig. 23a, a slice of fractal base F_1^8 is studied for $n = 3$, starting along the 8-duplicate of segment $A^1|\underline{C_{31}^a C_{32}^a}\{F_1^1\}$ shown in Fig. 24. As depicted in Fig. 29, the critical points with labels C_{33}^{a8}, C_{31}^{a8}, C_{31}^{b8} and C_{32}^{a8} are 8-duplicates of points C_{33}^a, C_{31}^a, C_{31}^b and C_{32}^a in Fig. 24, respectively. Recalling that C_{33} bifurcations only occur on stable parts, by intuition one may expect them to emerge on segment $A^8|\underline{C_{33}^{a8} C_{31}^{a8}}\{F_1^1\}$, where unfortunately none is found, probably due to the fact that the turning at this location is flipped upside-down when n decreases from ∞ to 3. Instead, the bifurcations are observed on the segment $A^8|\underline{C_{31}^{b8} C_{32}^{a8}}\{F_1^1\}$ which does not exist in the impacting system since it is part of the scattered grazing solution point $G_{2,4}^1$. Exactly $8 - 1 = 7$ C_{33} points are observed, among which C_{33}^b further leads to C_{33}^c, and the beginnings of the bifurcations at these points are plotted. Thus, a period-multiplying cascade can be tracked along the path marked in red and, similar to Fig. 23, a bifurcation diagram is generated to illustrate the cascade, as shown in Fig. 29, which is constructed by a Poincaré map where the displacements x_2 at the time instants $t = \frac{kT}{24} = \frac{2k\pi}{24\omega}, k = 1, 2, \ldots, 24$, are recorded for each solution point on the path, because the cascade eventually shows a $3 \times 2 \times 4 = 24$-time period multiplying. Note that when continuation is done for the periodic orbits of system (51) with $n = 3$, an additional constraint is applied so that the initial condition for x_2 is 0, as a result of which 0 is always recorded

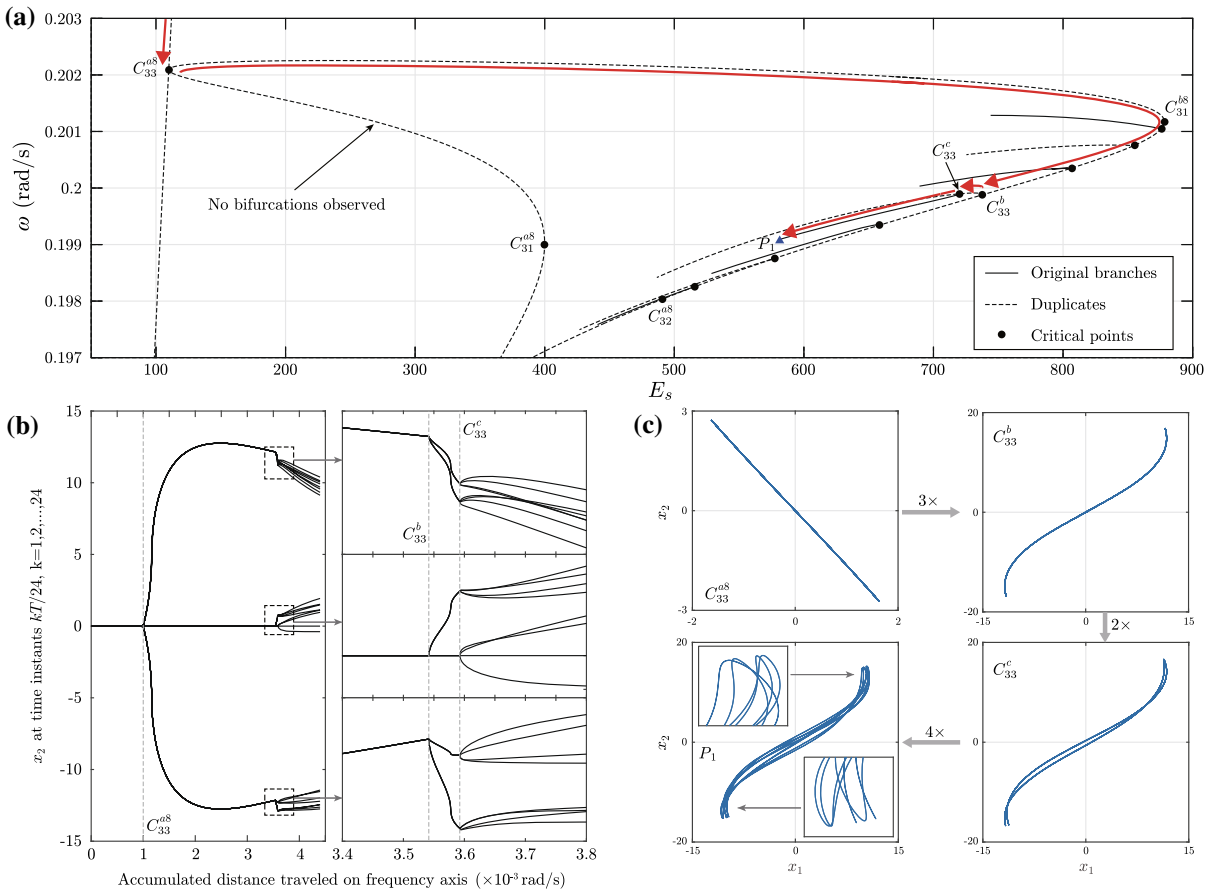

Fig. 29 An example of period-multiplying cascade at $n = 3$ in fractal base F_1^8: **a** FEP; **b** bifurcation diagram; **c** phase portraits at selected points

on the bifurcation diagram. At the same time, phase portraits at C_{33} points along the selected path as well as a temporary point P_1 selected as the end of the path are depicted in Fig. 29c.

In conclusion, nonlinear systems in the family defined by Equation (50) share similar FEP features. While some NNM sections show clear inheritance with varying order n, the grazing solution points in the impacting limit are scattered into critical points in systems with finite order n's. Meanwhile, the fractal structure consisted of cascades of period-multiplying bifurcations exists for both finite n's and $n \to \infty$. In general, the theoretical background of such bifurcations is briefly explained as follows. Along certain stable segments on the FEP, a pair of complex conjugate Floquet multipliers (as described in Sect. 2.4.2) travel along the unit circle on the complex plane so that they can be represented as $e^{\pm i2\pi\gamma}$, $\gamma \in \mathbb{R}$. Consider that at a solution point P there is $\gamma = p/q$, where p and q are coprime integers with $0 < p < q$. Then, the q-duplicate of P will have a pair of Floquet multipliers at 1, resulting in a q-time period-multiplying bifurcation. If the two Floquet multipliers each traverse the whole unit circle, then p has $q - 1$ possible values which naturally explains the previous observation of $k - 1$ bifurcations on a k-duplicate of certain segments. Since the distribution of solution points possessing rational γ's is dense on a given segment, when approaching zero frequency it will be infinitely rough, i.e., any fraction of the segment will include a C_{33} bifurcation in one of the fractal bases. Moreover, on a new stable segment that bifurcates out of this q-duplicate of P, the pair of Floquet multipliers of interest restart from 1 and again travel along the unit circle, resulting in cascades of such period-multiplying bifurcations. For instance, the evolution of two complex conjugate Flo-

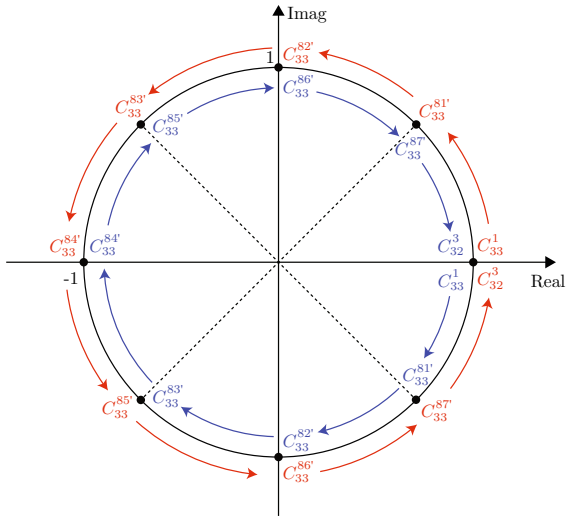

Fig. 30 The evolution of a pair of complex conjugate Floquet multipliers (in red and blue, respectively) on the unit circle along solution segment $S_6[010101]|\underline{C_{33}^1 C_{32}^3}$, with origins of the C_{33} points on its 8-duplicate labeled. (Color figure online)

quet multipliers along the segment $S_6[010101]|\underline{C_{33}^1 C_{32}^3}$ (which is original, as shown in Figs. 8 and 10) are depicted in Fig. 30. Denote the origins of critical points C_{33}^{8p}, $p = 1, 2, \ldots, 7$ (in Fig. 23) as $C_{33}^{8p'}$, which lie on $S_6[010101]|\underline{C_{33}^1 C_{32}^3}$, and the corresponding Floquet multipliers are exactly $e^{\pm i 2\pi \frac{p}{8}}$, as labeled in Fig. 30.

4 Conclusions

The periodic orbits of a 2-DOF conservative VI system are tracked by fitting the return map equations into the scheme of continuation. The method has shown satisfactory efficiency in that instead of involving numerical integrations in iterations, the equations are regular and explicit so that the continuation runs much faster. Meanwhile, it gives the exact solutions for systems with stereo-mechanical impact models instead of approximating the problem. Practically investigating critical and grazing solution points, in theory one can avoid missing any existing solution as long as it is somehow connected to any branch already found, either directly or to their multiple-period duplicates. A potential obstacle in implementation lies in that the shooting method may meet rank deficiency problems near critical points, due to numerical limitations, which in the future may be compensated by adopting pseudo-Newton methods.

It is illustrated that the FEP of the VI system experiences extremely complex trajectories due to period-multiplying bifurcations and complicated interactions among modes and their duplicates. It is shown that as a result the solutions develop in the form of infinite fractals so that the numerous cascades of period-multiplying bifurcations will lead to pseudo-periodic and likely chaotic responses that correspond to infinite periods and should lie at zero frequency on the FEP. Furthermore, it is shown that such fractal feature holds for counterpart systems with polynomial nonlinearities as well. However, though it is assumed that some of the stable branches of periodic solutions of such systems, when duplicated, can lead to an infinite number of bifurcations so that an infinite number of chaotic or pseudo-periodic responses can be located as the end of a cascade, it is not proved that any pseudo-periodic or chaotic response can be located in this way.

Acknowledgements This material is based upon work supported by the Purdue Research Foundation and the National Science Foundation under Grant No. CMMI 1662925.

Compliance with ethical standards

Conflict of interest The authors declare that they have no conflicts of interest.

References

1. Karayannis, I., Vakakis, A.F., Georgiades, F.: Vibro-impact attachments as shock absorbers. Proc. Inst. Mech. Eng. Part C J. Mech. Eng. Sci. **222**(10), 1899–1908 (2008)
2. Popplewell, N., Liao, M.: A simple design procedure for optimum impact dampers. J. Sound Vib. **146**(3), 519–526 (1991)
3. Brake, M.R.: The effect of the contact model on the impact-vibration response of continuous and discrete systems. J. Sound Vib. **332**(15), 3849–3878 (2013)
4. Blazejczyk-Okolewska, B., Czolczynski, K., Kapitaniak, T.: Classification principles of types of mechanical systems with impacts-fundamental assumptions and rules. Eur. J. Mech. A Solids **23**(3), 517–537 (2004)
5. Brogliato, B., Brogliato, B.: Nonsmooth Mechanics. Springer, Berlin (1999)
6. Van de Vorst, E.L.B., Van Campen, D.H., De Kraker, A., Fey, R.H.B.: Periodic solutions of a multi-dof beam system with impact. J. Sound Vib. **192**(5), 913–925 (1996)
7. Shaw, S.W., Holmes, P.J.: A periodically forced piecewise linear oscillator. J. Sound Vib. **90**(1), 129–155 (1983)
8. Shaw, S.W.: Forced vibrations of a beam with one-sided amplitude constraint: theory and experiment. J. Sound Vib. **99**(2), 199–212 (1985)

9. Moussi, E.H., Bellizzi, S., Cochelin, B., Nistor, I.: Nonlinear normal modes of a two degrees-of-freedom piecewise linear system. Mech. Syst. Signal Process. **64**, 266–281 (2015)
10. Blazejczyk-Okolewska, B., Czolczynski, K., Kapitaniak, T.: Dynamics of a two-degree-of-freedom cantilever beam with impacts. Chaos Solitons Fractals **40**(4), 1991–2006 (2009)
11. Czolczynski, K.: On the existence of a stable periodic solution of an impacting oscillator with damping. Chaos Solitons Fractals **19**(5), 1291–1311 (2004)
12. Aidanpää, J.-O., Gupta, R.B.: Periodic and chaotic behaviour of a threshold-limited two-degree-of-freedom system. J. Sound Vib. **165**(2), 305–327 (1993)
13. Budd, C., Dux, F., Cliffe, A.: The effect of frequency and clearance variations on single-degree-of-freedom impact oscillators. J. Sound Vib. **184**(3), 475–502 (1995)
14. Yue, Y., Xie, J.H.: Symmetry and bifurcations of a two-degree-of-freedom vibro-impact system. J. Sound Vib. **314**(1–2), 228–245 (2008)
15. Yue, Y.: Bifurcations of the symmetric quasi-periodic motion and lyapunov dimension of a vibro-impact system. Nonlinear Dyn. **84**(3), 1697–1713 (2016)
16. Masri, S.F.: Theory of the dynamic vibration neutralizer with motion-limiting stops. J. Appl. Mech. **39**(2), 563–568 (1972)
17. Pascal, M.: Dynamics and stability of a two degree of freedom oscillator with an elastic stop. J. Comput. Nonlinear Dyn. **1**(1), 94–102 (2006)
18. Nigm, M.M., Shabana, A.A.: Effect of an impact damper on a multi-degree of freedom system. J. Sound Vib. **89**(4), 541–557 (1983)
19. Rosenberg, R.M.: The normal modes of nonlinear n-degree-of-freedom systems. J. Appl. Mech. **29**(1), 7–14 (1962)
20. Shaw, S.W., Pierre, C.: Normal modes for non-linear vibratory systems. J. Sound Vib. **164**(1), 85–124 (1993)
21. Kerschen, G., Peeters, M., Golinval, J.-C., Vakakis, A.F.: Nonlinear normal modes, part I: a useful framework for the structural dynamicist. Mech. Syst. Signal Process. **23**(1), 170–194 (2009)
22. Pilipchuk, V.N.: The calculation of strongly non-linear systems close to vibration impact systems. J. Appl. Math. Mech. **49**(5), 572–578 (1985)
23. Pilipchuk, V.N.: Nonlinear Dynamics: Between Linear and Impact Limits, vol. 52. Springer, London (2010)
24. Lee, Y.S., Nucera, F., Vakakis, A.F., McFarland, D.M., Bergman, L.A.: Periodic orbits, damped transitions and targeted energy transfers in oscillators with vibro-impact attachments. Phys. D Nonlinear Phenom. **238**(18), 1868–1896 (2009)
25. Thorin, A., Delezoide, P., Legrand, M.: Nonsmooth modal analysis of piecewise-linear impact oscillators. SIAM J. Appl. Dyn. Syst. **16**(3), 1710–1747 (2017)
26. Zhao, X., Dankowicz, H., Reddy, C.K., Nayfeh, A.H.: Modeling and simulation methodology for impact microactuators. J. Micromech. Microeng. **14**(6), 775 (2004)
27. Kang, W., Thota, P., Wilcox, B., Dankowicz, H.: Bifurcation analysis of a microactuator using a new toolbox for continuation of hybrid system trajectories. J. Comput. Nonlinear Dyn. **4**(1), 011009 (2009)
28. Kerschen, G., Vakakis, A.F., Lee, Y.S., Mcfarland, D.M., Kowtko, J.J., Bergman, L.A.: Energy transfers in a system of two coupled oscillators with essential nonlinearity: 1: 1 resonance manifold and transient bridging orbits. Nonlinear Dyn. **42**(3), 283–303 (2005)
29. Lamarque, C.-H., Janin, O.: Modal analysis of mechanical systems with impact non-linearities: limitations to a modal superposition. J. Sound Vib. **235**, 567–609 (2000)
30. Jan, A., Claude-henri, L.: Bifurcation and Chaos in Nonsmooth Mechanical Systems, vol. 45. World Scientific, Singapore (2003)
31. Vakakis, A.F.: Nonlinear Targeted Energy Transfer in Mechanical and Structural Systems. Springer, Dordrecht (2009)
32. Banerjee, A., Das, R., Calius, E.P.: Vibration transmission through an impacting mass-in-mass unit: an analytical investigation. Int. J. Nonlinear Mech. **90**, 137–146 (2017)
33. Peeters, M., Viguié, R., Sérandour, G., Kerschen, G., Golinval, J.-C.: Nonlinear normal modes, part II: toward a practical computation using numerical continuation techniques. Mech. Syst. Signal Process. **23**(1), 195–216 (2009)
34. Nayfeh, A.H.: Applied Nonlinear Dynamics Analytical, Computational, and Experimental Methods. Wiley, New York (1995)
35. Polya, G., Read, R.C.: Combinatorial Enumeration of Groups, Graphs, and Chemical Compounds. Springer, Berlin (2012)
36. Kubicek, M., Marek, M.: Computational Methods in Bifurcation Theory and Dissipative Structures. Springer, Berlin (2012)